

Investigation of the Splitting of Quark and Gluon Jets

DELPHI Collaboration

Abstract

The splitting processes in identified quark and gluon jets are investigated using longitudinal and transverse observables. The jets are selected from symmetric three-jet events measured in Z decays with the DELPHI detector in 1991-1994. Gluon jets are identified using heavy quark anti-tagging.

Scaling violations in identified gluon jets are observed for the first time. The scale energy dependence of the gluon fragmentation function is found to be about two times larger than for the corresponding quark jets, consistent with the QCD expectation C_A/C_F .

The primary splitting of gluons and quarks into subjet agrees with fragmentation models and, for specific regions of the jet resolution y , with NLLA calculations. The maximum of the ratio of the primary subjet splittings in quark and gluon jets is $2.77 \pm 0.11 \pm 0.10$. Due to non-perturbative effects, the data are below the expectation at small y . The transition from the perturbative to the non-perturbative domain appears at smaller y for quark jets than for gluon jets. Combined with the observed behaviour of the higher rank splittings, this explains the relatively small multiplicity ratio between gluon and quark jets.

(Submitted to E. Phys. J. C)

P. Abreu²¹, W. Adam⁴⁹, T. Adye³⁶, P. Adzic¹¹, I. Ajinenko⁴¹, G. D. Alekseev¹⁶, R. Alemany⁴⁸, P. P. Allport²², S. Almedhed²⁴, U. Amaldi⁹, S. Amato⁴⁶, P. Andersson⁴³, A. Andreazza⁹, P. Antilogus²⁵, W.-D. Apel¹⁷, Y. Arnaud¹⁴, B. Åsman⁴³, J.-E. Augustin²⁵, A. Augustinus⁹, P. Baillon⁹, P. Bambade¹⁹, F. Barao²¹, R. Barbier²⁵, D. Y. Bardin¹⁶, G. Barker⁹, A. Baronecchi³⁹, O. Barring²⁴, M. J. Bates³⁶, M. Battaglia¹⁵, M. Baubillier²³, K.-H. Becks⁵¹, M. Begalli⁶, P. Beilliere⁸, Yu. Belokopytov^{9,52}, K. Belous⁴¹, A. C. Benvenuti⁵, C. Berat¹⁴, M. Berggren²⁵, D. Bertini²⁵, D. Bertrand², M. Besancon³⁸, F. Bianchi⁴⁴, M. Bigi⁴⁴, M. S. Bilenky¹⁶, P. Billoir²³, M.-A. Bizouard¹⁹, D. Bloch¹⁰, M. Bonesini²⁷, W. Bonivento²⁷, M. Boonekamp³⁸, P. S. L. Booth²², A. W. Borgland⁴, G. Borisov³⁸, C. Bosio³⁹, O. Botner⁴⁷, E. Boudinov³⁰, B. Bouquet¹⁹, C. Bourdarios¹⁹, T. J. V. Bowcock²², I. Bozovic¹¹, M. Bozzo¹³, P. Branchini³⁹, K. D. Brand³⁵, T. Brenke⁵¹, R. A. Brenner⁴⁷, R. Brown⁹, P. Bruckman³⁵, J.-M. Brunet⁸, L. Bugge³², T. Buran³², T. Burgsmueller⁵¹, P. Buschmann⁵¹, S. Cabrera⁴⁸, M. Caccia²⁷, M. Calvi²⁷, A. J. Camacho Rozas⁴⁰, T. Camporesi⁹, V. Canale³⁷, M. Canepa¹³, F. Carena⁹, L. Carroll²², C. Caso¹³, M. V. Castillo Gimenez⁴⁸, A. Cattai⁹, F. R. Cavallo⁵, Ch. Cerruti¹⁰, V. Chabaud⁹, M. Chapkin⁴¹, Ph. Charpentier⁹, L. Chaussard²⁵, P. Checchia³⁵, G. A. Chelkov¹⁶, M. Chen², R. Chierici⁴⁴, P. Chliapnikov⁴¹, P. Chochula⁷, V. Chorowicz²⁵, J. Chudoba²⁹, P. Crennell⁹, M. Colomei⁴⁸, R. Contri¹³, E. Cortina⁴⁸, G. Cosme¹⁹, F. Cossutti⁹, J.-H. Cowell²², H. B. Crawley¹, D. Crennell³⁶, G. Crosetti¹³, J. Cuevas Maestro³³, S. Czellar¹⁵, B. Dalmagne¹⁹, G. Damgaard²⁸, P. D. Dauncey³⁶, M. Davenport⁹, W. Da Silva²³, A. Deghorain², G. Della Ricca⁴⁵, P. Delpierre²⁶, N. Demaria⁹, A. De Angelis⁹, W. De Boer¹⁷, S. De Brabandere², C. De Clercq², C. De La Vaissiere²³, B. De Lotto⁴⁵, A. De Min³⁵, L. De Paula⁴⁶, H. Dijkstra⁹, L. Di Ciaccio³⁷, A. Di Diodato³⁷, A. Djannati⁸, J. Dolbeau⁸, K. Doroba⁵⁰, M. Dracos¹⁰, J. Drees⁵¹, K.-A. Drees⁵¹, M. Dris³¹, A. Duperrin²⁵, J.-D. Durand^{25,9}, D. Edsall¹, R. Ehret¹⁷, G. Eigen⁴, T. Ekelof⁴⁷, G. Ekspong⁴³, M. Ellert⁴⁷, M. Elsing⁹, J.-P. Engel¹⁰, B. Erzen⁴², M. Espirito Santo²¹, E. Falk²⁴, G. Fanourakis¹¹, D. Fassouliotis⁴⁵, J. Fayot²³, M. Feindt¹⁷, A. Fenyuk⁴¹, P. Ferrari²⁷, A. Ferrer⁴⁸, S. Fichet²³, A. Firestone¹, P.-A. Fischer⁹, U. Flagmeyer⁵¹, H. Foeth⁹, E. Fokitis³¹, F. Fontanelli¹³, F. Formenti⁹, B. Franek³⁶, A. G. Frodesen⁴, F. Fulda-Quenzer¹⁹, J. Fuster⁴⁸, A. Galloni²², D. Gamba⁴⁴, M. Gandelman⁴, C. Garcia⁴⁰, J. Garcia⁴⁰, C. Gaspar⁹, M. Gaspar⁴⁶, U. Gasparini³⁵, Ph. Gavillet⁹, E. N. Gazizov³¹, D. Gele¹⁰, J.-P. Gerber¹⁰, N. Ghodbane²⁵, F. Glege⁵¹, R. Gokiel⁵⁰, B. Golob⁴², P. Goncalves²¹, I. Gonzalez Caballero⁴⁰, G. Gopal³⁶, L. Gorn^{1,53}, M. Gorski⁵⁰, V. Gracco¹³, J. Grahl¹, E. Graziani³⁹, C. Green²², A. Grefrath⁵¹, P. Gris³⁸, G. Grosdidier¹⁹, K. Grzelak⁵⁰, M. Gunther⁴⁷, J. Guy³⁶, F. Hahn⁹, S. Hahn⁵¹, S. Haider⁹, Z. Hajduk¹⁸, A. Hallgren⁴⁷, K. Hamacher⁵¹, F. J. Harris³⁴, V. Hedberg²⁴, S. Heising¹⁷, R. Henriques²¹, J. J. Hernandez⁴⁸, P. Herquet², H. Herr⁹, T. L. Hessing³⁴, J.-M. Heuser⁵¹, E. Higon⁴⁸, S.-O. Holmgren⁴³, P. J. Holt³⁴, D. Holthuizen³⁰, S. Hoorelbeke², M. Houlden²², J. Hrubec⁴⁹, K. Huet², K. Hultqvist⁴³, J. N. Jackson²², R. Jacobsson⁴³, P. Jalocha⁹, R. Janik⁷, Ch. Jarlskog²⁴, G. Jarlskog²⁴, P. Jarry³⁸, B. Jean-Marie¹⁹, E. K. Johansson⁴³, L. Jonsson²⁴, P. Jonsson²⁴, C. Joram⁹, P. Juillot¹⁰, F. Kapusta²³, K. Karafasoulis¹¹, S. Katsanevas²⁵, E. C. Katsoufis³¹, R. Keranen⁴, Yu. Khokhlov⁴¹, B. A. Khomenko¹⁶, N. N. Khovanski¹⁶, B. King²², N. J. Kjaer³⁰, O. Klapp⁵¹, H. Klein⁹, P. Kluit³⁰, D. Knoblach¹⁷, P. Kokkinias¹¹, A. Konopliannikov⁴¹, M. Koratzinos⁹, K. Korcyl¹⁸, V. Kostioukhine⁴¹, C. Kourkoumelis³, O. Kouznetsov¹⁶, M. Krammer⁴⁹, C. Kreuter⁹, I. Kronkvist²⁴, Z. Krumstein¹⁶, P. Kubinec⁷, W. Kucewicz¹⁸, K. Kurvinen¹⁵, C. Lacasta⁹, J. W. Lamsa¹, L. Lanceri⁴⁵, D. W. Lane¹, P. Langefeld⁵¹, J.-P. Laugier³⁸, R. Lauhakangas¹⁵, G. Leder⁴⁹, F. Ledroit¹⁴, V. Lefebvre², C. K. Legan¹, A. Leisos¹¹, R. Leitner²⁹, J. Lemonne², G. Lenzen⁵¹, V. Lepeltier¹⁹, T. Lesiak¹⁸, M. Lethuillier³⁸, J. Libby³⁴, D. Liko⁹, A. Lipniacka⁴³, I. Lippi³⁵, B. Loerstad²⁴, J. G. Loken³⁴, J. H. Lopes⁴⁶, J. M. Lopez⁴⁰, D. Loukas¹¹, P. Lutz³⁸, L. Lyons³⁴, J. MacNaughton⁴⁹, G. Maehlum¹⁷, J. R. Mahon⁶, A. Maio²¹, A. Malek⁵¹, T. G. M. Malmgren⁴³, V. Malychiev¹⁶, F. Mandl⁴⁹, J. Marco⁴⁰, R. Marco⁴⁰, B. Marechal⁴⁶, M. Margoni³⁵, J.-C. Marin⁹, C. Mariotti⁹, A. Markou¹¹, C. Martinez-Rivero³³, F. Martinez-Vidal⁴⁸, S. Marti i Garcia²², J. Masik²⁹, F. Matorras⁴⁰, C. Matteuzzi²⁷, G. Matthiae³⁷, F. Mazzucato³⁵, M. Mazzucato³⁵, M. Mc Cubbin²², R. Mc Kay¹, R. Mc Nulty⁹, G. Mc Pherson²², J. Medbo⁴⁷, C. Meroni²⁷, W. T. Meyer¹, A. Miagkov⁴¹, M. Michelotto³⁵, E. Migliore⁴⁴, L. Mirabito²⁵, W. A. Mitaroff⁴⁹, U. Mjoernmark²⁴, T. Moa⁴³, R. Moeller²⁸, K. Moenig⁹, M. R. Monge¹³, X. Moreau²³, P. Morettini¹³, H. Mueller¹⁷, K. Muenich⁵¹, M. Mulders³⁰, L. M. Mundim⁶, W. J. Murray³⁶, B. Muryn^{14,18}, G. Myatt³⁴, T. Myklebust³², F. Naraghi¹⁴, F. L. Navarria⁵, S. Navas⁴⁸, K. Nawrocki⁵⁰, P. Negri²⁷, S. Nemecek¹², N. Neufeld⁹, W. Neumann⁵¹, N. Neumeister⁴⁹, R. Nicolaidou¹⁴, B. S. Nielsen²⁸, M. Nieuwenhuizen³⁰, V. Nikolaenko¹⁰, M. Nikolenko^{10,16}, P. Niss⁴³, A. Nomerotski³⁵, A. Normand²², A. Nygren²⁴, W. Oberschulte-Beckmann¹⁷, V. Obraztsov⁴¹, A. G. Olshevski¹⁶, A. Onofre²¹, R. Orava¹⁵, G. Orazi¹⁰, K. Osterberg¹⁵, A. Ouraou³⁸, P. Paganini¹⁹, M. Paganoni²⁷, S. Paiano⁵, R. Pain²³, R. Paiva²¹, H. Palka¹⁸, Th. D. Papadopoulou³¹, K. Papageorgiou¹¹, L. Pape⁹, C. Parkes³⁴, F. Parodi¹³, U. Parzefall²², A. Passeri³⁹, M. Pegoraro³⁵, L. Peralta²¹, H. Pernegger⁴⁹, M. Pernicka⁴⁹, A. Perrotta⁵, C. Petridou⁴⁵, A. Petrolini¹³, H. T. Phillips³⁶, G. Piana¹³, F. Pierre³⁸, M. Pimenta²¹, E. Piotto³⁵, T. Podobnik³⁴, O. Podobrin⁹, M. E. Pol⁶, G. Polok¹⁸, P. Poropat⁴⁵, V. Pozdniakov¹⁶, P. Privitera³⁷, N. Pukhaeva¹⁶, A. Pullia²⁷, D. Radojicic³⁴, S. Ragazzi²⁷, H. Rahmani³¹, P. N. Ratoff²⁰, A. L. Read³², P. Rebecchi⁹, N. G. Redaelli²⁷, M. Regler⁴⁹, D. Reid⁹, R. Reinhardt⁵¹, P. B. Renton³⁴, L. K. Resvanis³, F. Richard¹⁹, J. Ridky¹², G. Rinaudo⁴⁴, O. Rohne³², A. Romero⁴⁴, P. Ronchese³⁵, E. I. Rosenberg¹, P. Rosinsky⁷, P. Roudeau¹⁹, T. Rovelli⁵, V. Ruhlmann-Kleider³⁸, A. Ruiz⁴⁰, H. Saarikko¹⁵, Y. Sacquin³⁸, A. Sadovskiy¹⁶, G. Sajot¹⁴, J. Salt⁴⁸, D. Sampsonidis¹¹, M. Sannino¹³, H. Schneider¹⁷, U. Schwicklerath¹⁷, M. A. E. Schyns⁵¹, F. Scuri⁴⁵, P. Seager²⁰, Y. Sedykh¹⁶, A. M. Segar³⁴, R. Sekulin³⁶, R. C. Shellard⁶, A. Sheridan²², R. Silvestre³⁸, F. Simonetto³⁵, A. N. Sisakian¹⁶, T. B. Skaali³², G. Smadja²⁵, O. Smirnova²⁴, G. R. Smith³⁶, A. Sokolov⁴¹, O. Solovianov⁴¹, A. Sopczak¹⁷, R. Sosnowski⁵⁰, D. Souza-Santos⁶, T. Spassov²¹, E. Spiriti³⁹, P. Sponholz⁵¹, S. Squarcia¹³, D. Stampfer⁹, C. Stanescu³⁹, S. Stanic⁴², S. Stapnes³², I. Stavitski³⁵, K. Stevenson³⁴, A. Stocchi¹⁹, J. Strauss⁴⁹, R. Strub¹⁰, B. Stugu⁴, M. Szczekowski⁵⁰, M. Szeptycka⁵⁰

T.Tabarelli²⁷, F.Tegenfeldt⁴⁷, F.Terranova²⁷, J.Thomas³⁴, A.Tilquin²⁶, J.Timmermans³⁰, L.G.Tkatchev¹⁶, T.Todorov¹⁰, S.Todorova¹⁰, D.Z.Toet³⁰, A.Tomaradze², B.Tome²¹, A.Tonazzo²⁷, L.Tortora³⁹, G.Transtrome²⁴, D.Treille⁹, G.Tristram⁸, A.Trombini¹⁹, C.Troncon²⁷, A.Tsirou⁹, M-L.Turluer³⁸, I.A.Tyapkin¹⁶, M.Tyndel³⁶, S.Tzamaras¹¹, B.Ueberschaer⁵¹, O.Ullaland⁹, V.Uvarov⁴¹, G.Valenti⁵, E.Vallazza⁴⁵, C.Vander Velde², G.W.Van Apeldoorn³⁰, P.Van Dam³⁰, W.K.Van Doninck², J.Van Eldik³⁰, A.Van Lysebetten², I.Van Vulpen³⁰, N.Vassilopoulos³⁴, G.Vegni²⁷, L.Ventura³⁵, W.Venus³⁶, F.Verbeure², M.Verlato³⁵, L.S.Vertogradov¹⁶, V.Verzi³⁷, D.Vilanova³⁸, P.Vincent²³, L.Vitale⁴⁵, A.S.Vodopyanov¹⁶, V.Vrba¹², H.Wahlen⁵¹, C.Walck⁴³, F.Waldner⁴⁵, C.Weiser¹⁷, A.M.Wetherell⁹, D.Wicke⁵¹, J.H.Wickens², M.Wielers¹⁷, G.R.Wilkinson⁹, W.S.C.Williams³⁴, M.Winter¹⁰, M.Witek¹⁸, T.Wlodek¹⁹, G.Wolf⁹, J.Yi¹, O.Yushchenko⁴¹, A.Zaitsev⁴¹, A.Zalewska¹⁸, P.Zalewski⁵⁰, D.Zavrtanik⁴², E.Zevgolatakis¹¹, N.I.Zimin¹⁶, G.C.Zucchelli⁴³, G.Zumerle³⁵

¹Department of Physics and Astronomy, Iowa State University, Ames IA 50011-3160, USA

²Physics Department, Univ. Instelling Antwerpen, Universiteitsplein 1, BE-2610 Wilrijk, Belgium and IIHE, ULB-VUB, Pleinlaan 2, BE-1050 Brussels, Belgium

and Faculté des Sciences, Univ. de l'Etat Mons, Av. Maistriau 19, BE-7000 Mons, Belgium

³Physics Laboratory, University of Athens, Solonos Str. 104, GR-10680 Athens, Greece

⁴Department of Physics, University of Bergen, Allégaten 55, NO-5007 Bergen, Norway

⁵Dipartimento di Fisica, Università di Bologna and INFN, Via Irnerio 46, IT-40126 Bologna, Italy

⁶Centro Brasileiro de Pesquisas Físicas, rua Xavier Sigaud 150, BR-22290 Rio de Janeiro, Brazil

and Depto. de Física, Pont. Univ. Católica, C.P. 38071 BR-22453 Rio de Janeiro, Brazil

and Inst. de Física, Univ. Estadual do Rio de Janeiro, rua São Francisco Xavier 524, Rio de Janeiro, Brazil

⁷Comenius University, Faculty of Mathematics and Physics, Mlynska Dolina, SK-84215 Bratislava, Slovakia

⁸Collège de France, Lab. de Physique Corpusculaire, IN2P3-CNRS, FR-75231 Paris Cedex 05, France

⁹CERN, CH-1211 Geneva 23, Switzerland

¹⁰Institut de Recherches Subatomiques, IN2P3 - CNRS/ULP - BP20, FR-67037 Strasbourg Cedex, France

¹¹Institute of Nuclear Physics, N.C.S.R. Demokritos, P.O. Box 60228, GR-15310 Athens, Greece

¹²FZU, Inst. of Phys. of the C.A.S. High Energy Physics Division, Na Slovance 2, CZ-180 40, Praha 8, Czech Republic

¹³Dipartimento di Fisica, Università di Genova and INFN, Via Dodecaneso 33, IT-16146 Genova, Italy

¹⁴Institut des Sciences Nucléaires, IN2P3-CNRS, Université de Grenoble 1, FR-38026 Grenoble Cedex, France

¹⁵Helsinki Institute of Physics, HIP, P.O. Box 9, FI-00014 Helsinki, Finland

¹⁶Joint Institute for Nuclear Research, Dubna, Head Post Office, P.O. Box 79, RU-101 000 Moscow, Russian Federation

¹⁷Institut für Experimentelle Kernphysik, Universität Karlsruhe, Postfach 6980, DE-76128 Karlsruhe, Germany

¹⁸Institute of Nuclear Physics and University of Mining and Metallurgy, Ul. Kawiora 26a, PL-30055 Krakow, Poland

¹⁹Université de Paris-Sud, Lab. de l'Accélérateur Linéaire, IN2P3-CNRS, Bât. 200, FR-91405 Orsay Cedex, France

²⁰School of Physics and Chemistry, University of Lancaster, Lancaster LA1 4YB, UK

²¹LIP, IST, FCUL - Av. Elias Garcia, 14-1^o, PT-1000 Lisboa Codex, Portugal

²²Department of Physics, University of Liverpool, P.O. Box 147, Liverpool L69 3BX, UK

²³LPNHE, IN2P3-CNRS, Univ. Paris VI et VII, Tour 33 (RdC), 4 place Jussieu, FR-75252 Paris Cedex 05, France

²⁴Department of Physics, University of Lund, Sölvegatan 14, SE-223 63 Lund, Sweden

²⁵Université Claude Bernard de Lyon, IPNL, IN2P3-CNRS, FR-69622 Villeurbanne Cedex, France

²⁶Univ. d'Aix - Marseille II - CPP, IN2P3-CNRS, FR-13288 Marseille Cedex 09, France

²⁷Dipartimento di Fisica, Università di Milano and INFN, Via Celoria 16, IT-20133 Milan, Italy

²⁸Niels Bohr Institute, Blegdamsvej 17, DK-2100 Copenhagen Ø, Denmark

²⁹NC, Nuclear Centre of MFF, Charles University, Areal MFF, V Holesovickach 2, CZ-180 00, Praha 8, Czech Republic

³⁰NIKHEF, Postbus 41882, NL-1009 DB Amsterdam, The Netherlands

³¹National Technical University, Physics Department, Zografou Campus, GR-15773 Athens, Greece

³²Physics Department, University of Oslo, Blindern, NO-1000 Oslo 3, Norway

³³Dpto. Física, Univ. Oviedo, Avda. Calvo Sotelo s/n, ES-33007 Oviedo, Spain, (CICYT-AEN96-1681)

³⁴Department of Physics, University of Oxford, Keble Road, Oxford OX1 3RH, UK

³⁵Dipartimento di Fisica, Università di Padova and INFN, Via Marzolo 8, IT-35131 Padua, Italy

³⁶Rutherford Appleton Laboratory, Chilton, Didcot OX11 0QX, UK

³⁷Dipartimento di Fisica, Università di Roma II and INFN, Tor Vergata, IT-00173 Rome, Italy

³⁸DAPNIA/Service de Physique des Particules, CEA-Saclay, FR-91191 Gif-sur-Yvette Cedex, France

³⁹Istituto Superiore di Sanità, Ist. Naz. di Fisica Nucl. (INFN), Viale Regina Elena 299, IT-00161 Rome, Italy

⁴⁰Instituto de Física de Cantabria (CSIC-UC), Avda. los Castros s/n, ES-39006 Santander, Spain, (CICYT-AEN96-1681)

⁴¹Inst. for High Energy Physics, Serpukov P.O. Box 35, Protvino, (Moscow Region), Russian Federation

⁴²J. Stefan Institute, Jamova 39, SI-1000 Ljubljana, Slovenia and Department of Astroparticle Physics, School of Environmental Sciences, Kostanjevska 16a, Nova Gorica, SI-5000 Slovenia, and Department of Physics, University of Ljubljana, SI-1000 Ljubljana, Slovenia

⁴³Fysikum, Stockholm University, Box 6730, SE-113 85 Stockholm, Sweden

⁴⁴Dipartimento di Fisica Sperimentale, Università di Torino and INFN, Via P. Giuria 1, IT-10125 Turin, Italy

⁴⁵Dipartimento di Fisica, Università di Trieste and INFN, Via A. Valerio 2, IT-34127 Trieste, Italy and Istituto di Fisica, Università di Udine, IT-33100 Udine, Italy

⁴⁶Univ. Federal do Rio de Janeiro, C.P. 68528 Cidade Univ., Ilha do Fundão BR-21945-970 Rio de Janeiro, Brazil

⁴⁷Department of Radiation Sciences, University of Uppsala, P.O. Box 535, SE-751 21 Uppsala, Sweden

⁴⁸IFIC, Valencia-CSIC, and D.F.A.M.N., U. de Valencia, Avda. Dr. Moliner 50, ES-46100 Burjassot (Valencia), Spain

⁴⁹Institut für Hochenergiephysik, Österr. Akad. d. Wissensch., Nikolsdorfergasse 18, AT-1050 Vienna, Austria

⁵⁰Inst. Nuclear Studies and University of Warsaw, Ul. Hoza 69, PL-00681 Warsaw, Poland

⁵¹Fachbereich Physik, University of Wuppertal, Postfach 100 127, DE-42097 Wuppertal, Germany

⁵²On leave of absence from IHEP Serpukhov

⁵³Now at University of Florida

1 Introduction

The dynamics of the strong interaction are described by Quantum Chromodynamics, QCD, a non-Abelian gauge theory. This theory contains two types of fundamental fields, the quarks which are fermions and the self-interacting gluons, the vector bosons which mediate the strong force. Quarks and gluons are not directly observable, but they give rise to narrow bunches of hadrons called jets. In our present understanding, these jets result from a showering process, i.e. a chain of elementary splitting processes of the initial quarks or gluons.

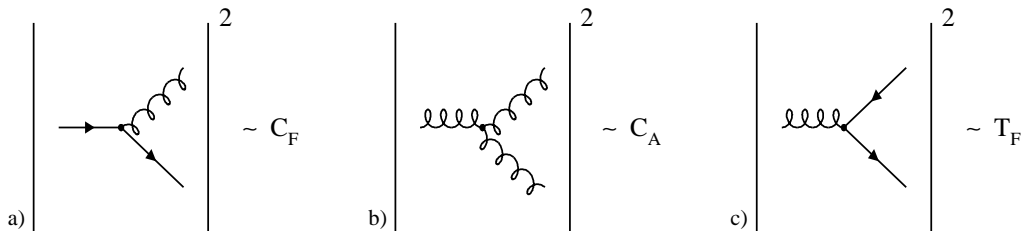


Figure 1: Diagrams of the fundamental QCD couplings

The relative strengths of these splittings are determined by the colour factors (also called Casimir factors) which are determined by the structure of $SU(3)$, the group underlying QCD. As shown in Fig. 1, the colour factors C_F , C_A , and T_F respectively determine the coupling strengths of gluon radiation from quarks, of gluon radiation from gluons (the triple-gluon vertex) and of gluon splitting into a quark-antiquark pair. Within $SU(3)$, these coupling constants are $C_F = 4/3$, $C_A = 3$, and $T_F = 1/2$, which has to be weighted by the number of active quark flavors n_F . However, gluon splitting into a quark-antiquark pair is also dynamically suppressed.

In QCD $\frac{C_A}{C_F} = \frac{9}{4}$, so more splittings are expected in gluon jets than in quark jets. Consequently, gluon and quark jets should be substantially different. In particular one naïvely expects the ratio $\frac{n_g}{n_q}$ of the hadron multiplicities in gluon and quark jets to be approximately $\frac{C_A}{C_F}$ [1]. This expectation is essentially maintained in more elaborate calculations [2].

Experimentally, however, the observed differences between quark and gluon jets are small. In three-jet events in e^+e^- annihilation at Z energies, n_g/n_q is measured to be about 1.25 [3,4]. An increase of this ratio with energy has been demonstrated in a previous paper [3] and meanwhile confirmed [5].

It is important to clarify and understand the origin of the obvious discrepancy between the experimental findings and the naïve QCD expectation.

The aims of this paper are

- to establish that the initial splittings in quark and gluon jets are indeed consistent with the QCD expectations and
- to study the jet evolution in order to understand and explain the observed small difference in particle multiplicities in quark and gluon jets.

To achieve these objectives, two different types of observables are used. These are: a) the scale dependence of the scaled energy distribution of stable hadrons, sensitive mainly to the longitudinal part of the jet evolution, and b) the subjet splittings as defined by the Durham jet finder, related mainly to the transverse momentum of the splitting processes. The latter also provide a direct test of the splitting kernels and the Sudakov form factors for quarks and gluons, the bases of parton shower evolution. Finally, the numbers of subjets originating from initial quarks and gluons are compared.

Quark and gluon jets are selected in symmetric three-jet events. Gluon jets are identified using heavy quark anti-tagging. The definition of a quark or gluon jet relies on the analogy to tree level graphs. Higher order corrections affect this identification by terms of order $\mathcal{O}(\alpha_S)$. As the interest of this paper is mainly to achieve qualitative understanding, these subtleties are ignored.

Section 2 of this paper describes the experimental details. The study of the scale dependence of the fragmentation function is presented in section 3 and that of subjet splittings in section 4. The systematic errors are discussed in section 5. The conclusions are summarized in section 6.

2 Experimental Apparatus and Event Selection

This section describes the parts of the DELPHI detector relevant to this analysis, the particle and event selection, the jet reconstruction, the event topologies analysed, the impact parameter tagging used for selecting gluon and quark jet samples, and the subtraction method used to extract the properties of pure light-quark and gluon jet samples.

2.1 The Delphi Detector

A detailed description of the DELPHI apparatus and its performance during the years 1991 to 1994 is presented in [6,7].

The main part of the tracking system was a 2.7 m long Time Projection Chamber (*TPC*) within a magnetic field which measured the tracks of charged particles with a resolution of about 250 μm in the $R\phi$ projection (transverse to the beam direction) and 0.9 mm along the z direction (beam direction). The space between the *TPC* and the beam pipe contained the Inner Detector (*ID*) and a silicon microstrip Vertex Detector (*VD*). Each 15° sector of the *ID* consisted of a 24 wire jet chamber followed by a 5 layer proportional chamber. The Vertex Detector consisted of three concentric shells of 24 silicon microstrip detector modules each 24 cm long. Its very good spatial resolution (7.6 μm in $R\phi$ in all years, and 9-30 μm in z in 1994) made it the most important component of DELPHI for the reconstruction of vertices and for the impact parameter tag. In the barrel region (polar angle θ relative to the beam axis between 43° and 137°), the quality of tracking was further improved by the Outer Detector containing 5 layers of drift tubes. Each layer measured the $R\phi$ -coordinate with a resolution of about 110 μm . Three layers also provided an approximate z measurement with a resolution of 4 cm.

Two additional drift chamber systems improved the tracking acceptance in the forward and backward regions (θ in the range $11^\circ - 33^\circ$ or $147^\circ - 169^\circ$). Forward chamber *A* (*FCA*) consisted of three pairs of wire planes rotated by 120° with respect to each other, in order to resolve ambiguities internally. Forward chamber *B* (*FCB*) consisted of 12 wire planes twice repeating the orientations of *FCA* and positioned directly in front of the forward electromagnetic calorimeter (*FEMC*).

Electromagnetic clusters were measured in the barrel region by a High Density Projection Chamber (*HPC*) and in the forward region (θ in the range $10^\circ - 36.5^\circ$ or $143.5^\circ - 170^\circ$) by the Forward ElectroMagnetic Calorimeter *FEMC*. The Hadron Calorimeter (*HAC*), embedded in the iron magnetic return yoke outside the electromagnetic calorimeter and magnetic coil, provided energy and position measurements for neutral hadrons.

2.2 Particle and Event Selection

All data collected by DELPHI during the years 1991 to 1994 are considered in the present analysis. In a first step of the selection procedure, the quality cuts given in Tables 1 and 2 are imposed on all charged particles and on all neutral particles detected in the calorimeters respectively, in order to ensure a reliable determination of their momenta, energies, and multiplicities.

Variable	Cuts
Momentum, p	$\geq 0.4 \text{ GeV}/c$
Polar angle, θ	$20^\circ - 160^\circ$
Impact parameter, $\epsilon_{R\phi}$	$\leq 5.0 \text{ cm}$
Impact parameter, ϵ_z	$\leq 10.0 \text{ cm}$
Track length, L_{track}	$\geq 30 \text{ cm}$
Momentum error, $\frac{\Delta p}{p}$	$\leq 100\%$

Table 1: Track selection for charged particles

Detector	$E_{min} [\text{GeV}]$	$E_{max} [\text{GeV}]$
HPC	0.5	50
FEMC	0.5	30
HAC	1.0	50

Table 2: Energy cuts for neutral particles

All charged particles are assumed to be pions and all neutral particles are assumed massless. A sample of hadronic events is then selected as in [3,8] using the cuts shown in Table 3. These demand a minimum charged multiplicity, N_{ch} , and a minimum visible energy carried by charged particles, E_{ch}^{tot} , as well as requiring the events to be well contained within the detector. E_{ch}^{hemi} denotes the sum of the energies of charged particles in the forward or backward hemisphere of the DELPHI detector. An event is discarded if the momentum of one of its charged particles is greater than p_{max} . The resulting hadronic event samples are listed in Table 5.

Variable	Cut
N_{ch}	≥ 5
E_{ch}^{tot}	$\geq 0.15 \sqrt{s}$
$\theta_{Sphericity}$	$30^\circ - 150^\circ$
E_{ch}^{hemi}	$\geq 0.03 \sqrt{s}$
p_{max}	$45 \text{ GeV}/c$

Table 3: Hadronic event selection

2.3 The Jet Finding Algorithm

A three-jet event sample is selected using the k_\perp jet clustering algorithm [9], originally known as the Durham jet finder. In this scheme, a jet resolution variable y_{ij} is defined for every pair of particles i and j in an event by:

$$y_{ij} = \frac{2 \cdot \min(E_i^2, E_j^2) \cdot (1 - \cos \Theta_{ij})}{E_{vis}^2} \quad (1)$$

where E_i and E_j are the energies of particles i and j , Θ_{ij} is the angle between them, and E_{vis} is the sum of all measured particle energies in the event. If the lowest value of y_{ij} is below y_{cut} , the corresponding particle pair is replaced by a pseudo-particle with the sum of their four-momenta, $p_{ij} = p_i + p_j$.

The procedure is then repeated, re-evaluating the jet resolution variables in each iteration, until all pairs i and j satisfy $y_{ij} > y_{cut}$. Each four-momentum vector remaining at the end of this process is referred to as a ‘‘jet’’. With this algorithm, the minimum transverse momentum between two jets, resolved at a scale defined by y_{cut} , is approximately given by $k_\perp^{min} \simeq E_{vis} \sqrt{y_{cut}}$.

The k_\perp algorithm conserves both energy and momentum, is well suited for perturbative calculations, and avoids the recombination of soft gluons in different hemispheres of the event.

2.4 Event Topologies

After the hadronic event selection, the k_\perp cluster algorithm is applied to select three-jet final states using $y_{cut} = 0.015$. This value maximizes the three-jet event sample and allows reliable comparison with perturbative QCD.

A detailed comparison of quark and gluon jet properties needs samples of quark and gluon jets with nearly the same kinematics to allow a direct comparison of their properties within a similar environment. To fulfil this condition, two different event topologies have been used, as illustrated in Fig. 2:

- mirror symmetric events, with θ_2 and $\theta_3 \in [150^\circ - 15^\circ, 150^\circ + 15^\circ]$, subsequently called **Y events**, and
- three-fold symmetric events, with θ_2 and $\theta_3 \in [120^\circ - 15^\circ, 120^\circ + 15^\circ]$, subsequently called **Mercedes events**.

The jet axes are projected into the event plane, which is defined by the plane perpendicular to the smallest sphericity eigenvector as obtained from the quadratic momentum

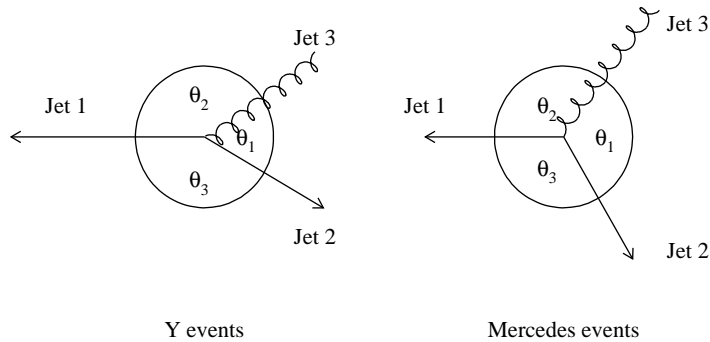


Figure 2: Event topologies of symmetric Y events and Mercedes events; θ_i are the angles between the jets after projection into the event plane.

tensor. The energy of each jet is then calculated from the angles between the jets assuming massless kinematics, using:

$$E_j^{calc} = \frac{\sin\theta_j}{\sin\theta_1 + \sin\theta_2 + \sin\theta_3} \sqrt{s}, \quad j = 1, 2, 3, \quad (2)$$

where θ_j is the interjet angle as defined in Fig. 2.

In order to enhance the contribution from events with three well defined jets attributable to $q\bar{q}g$ production, further cuts are then applied as summarized in Table 4. These cuts select planar events with each of the reconstructed jets well contained within the sensitive part of the detector.

Measurement	Cuts
Number of particles in each jet	≥ 2 (charged or neutral)
Visible jet energy per jet	≥ 5 GeV
Sum of angles between jets	$\geq 355^\circ$
Polar angle of each jet axis	$30^\circ - 150^\circ$

Table 4: Planarity and acceptance cuts for reconstructed jets.

The numbers of events remaining after applying this selection procedure to the initial $\sim 3,040,000$ hadronic events collected by DELPHI in 1991-1994 and to $\sim 7,940,000$ corresponding simulated events are given in Table 5.

2.5 Quark and Gluon Jet Identification

A sample rich in gluon jets is obtained from 3-jet events which originate from Z decays to a $b\bar{b}$ pair. The events are identified (see section 2.5.1) using a lifetime-tag technique, and the gluon jets are tagged indirectly by identifying the other two jets as b -quark jets using the lifetime-tag.

The light (udsc) quark jets used for comparison to these gluon jets are taken from events failing the event level lifetime-tag. These events contain two jets of similar topology

	Y events		Mercedes events		Hadronic events	
Year	Data	Simulation	Data	Simulation	Data	Simulation
1991	12839	19080	1399	2152	250760	347941
1992	36074	147563	3901	16543	699704	2641058
1993	36398	98782	4038	10771	704669	1760449
1994	70654	213683	7927	24078	1383821	3191588
total	155965	479108	17265	53544	3038954	7941036

Table 5: Samples of selected Y and Mercedes events and the initial hadronic event samples.

in the case of Y events, and three jets in the case of Mercedes events. These jet samples are subsequently called “normal mixture”¹.

In effect, subtracting the small residual heavy quark contributions from the tagged sample yields the pure gluon sample. The properties of light-quark jets are obtained by subtracting the gluon distributions from the distributions measured in the normal mixture jet sample.

In this way neither the gluon nor the light-quark distributions are significantly biased by the identification procedure. However the jets identified as b -quark jets are biased. More importantly, about half of the particles in b jets come from the weak decays of B hadrons. Thus b jets cannot be used for a direct comparison with gluon jets within a purely QCD framework neglecting these decays.

In the following, the selection of the gluon and the normal mixture jet samples in Y- and Mercedes events is described in detail as well as the corrections applied to obtain information on pure quark and gluon jets.

2.5.1 Lifetime Tags at Event and Jet Level

The lifetime signed impact parameters and their error distributions are used to construct an algorithm for tagging b jets [7,10]. In this method, the probability, P_N , for the hypothesis that all tracks arise directly from the e^+e^- annihilation point is evaluated for a given selection of N tracks. By construction, light-quark events or jets have a flat distribution in P_N while, because of the long lifetimes of B hadrons, events or jets containing b quarks tend to give low values.

Events with a b quark signature are selected as input to the gluon identification by demanding that P_E , the value of P_N evaluated for the whole event, does not exceed $10^{-1.5}$.

The tracks corresponding to each of the reconstructed jets are then used to construct a probability P_J per jet. Jets are finally classified according to the observed values of P_J following two selection strategies:

- I. As the most energetic jet in Y events is a quark jet in about 98% of the cases, this jet is treated as a quark jet in every Y event. Cuts on P_J are applied to each of the two lower energy jets in order to decide which is the quark jet and which is the gluon

¹“Normal mixture” denotes the intrinsic mixture of the similar-topology jets within the selected events, namely the two low energy jets in Y events (usually one quark and one gluon jet) and all three jets in Mercedes events (always two quark and one gluon jet) rather than the mixture of the initial quarks in these events predicted by the Standard Model.

jet. The main criterion applied is to demand that one of the two lower energy jets satisfies the condition $P_J < 0.1$. The remaining jet is then taken as the gluon jet provided its probability value P_J is above 0.1. This ensures that the decay products of the b hadrons do not, in general, filter through to the selected sample of gluon jets. In total, 18545 gluon jets in Y type events are selected using this single jet tag method.

- II. For Mercedes type events, both of the quark jets have to be identified by applying cuts to the jet probability variable, as all of the three jets have comparable energy. By demanding that two of the three jets satisfy the condition $P_J < 0.1$, the remaining jet is then considered as the gluon jet provided its probability value P_J exceeds 0.1. A total of 1203 gluon jets are identified in Mercedes events using this double jet tag method.

In Fig. 3, the probability distributions of the jets, P_J , in Y events are shown separately for normal mixture jets, charm jets, b quark jets, and gluon jets.

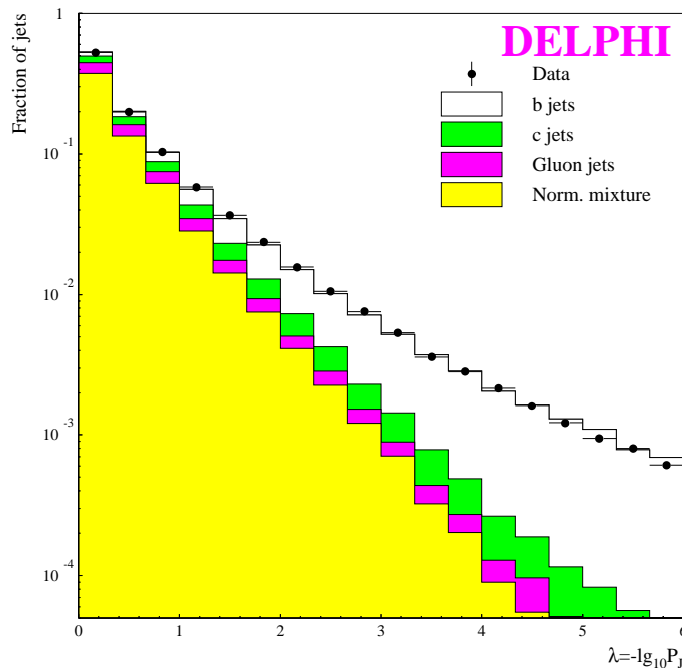


Figure 3: Jet probabilities for normal mixture (in uds events), c quark, b quark, and gluon jets (in c and b events)

2.5.2 Gluon and Quark Jet Purities

The efficiency and purity calculations have been made using events generated by the JETSET 7.3 Monte Carlo [11] tuned to DELPHI data [12], passed through the full simulation program DELSIM [13,7] of the DELPHI detector and the standard DELPHI data reconstruction chain.

Even in simulated events, the assignment of parton flavours to the jets is not unique, as the decay history is interrupted by the building of strings in models like JETSET or of

clusters in the case of HERWIG [14]. Thus two independent ways of defining the gluon jet in the fully simulated events are investigated [8]. On the one hand it is assumed that the jet which has the largest angle to hadrons containing heavy quarks will be the gluon induced jet ² (angle assignment), on the other hand the jet containing the fewest decay particles from the heavy hadrons is assigned to the gluon (history assignment). Table 6 shows that the methods give similar results and that therefore the purities can be estimated with small systematic uncertainties. With the tagging procedure described in section 2.5.1, gluon jet purities ³ of $(79.6 \pm 2.0)\%$ (Y events) and $(74.5 \pm 2.5)\%$ (Mercedes events) were achieved (an estimate of the systematic error is included in the quoted errors).

Method	Angle assignment			
	gluon in:	Jet 1	Jet 2	Jet 3
History assignment	Jet 1	5.3%	0.05%	0.09%
	Jet 2	0.01%	34%	0.50%
	Jet 3	0.02%	0.71%	60%

Table 6: Correlation of angle and history assignments in simulated data after application of the selections given in Tables 1-4. The jets are numbered in order of decreasing energy. The table has been obtained for arbitrary three-jet events with $\theta_2, \theta_3 \in [110^\circ, 170^\circ]$. These events contain the Y- and Mercedes events.

2.5.3 Corrections

Table 7 shows in detail the fractions in Y events of light (*udsc*) quark, *b* quark, and gluon jets in the three different jet classes, namely normal mixture jets, *b* tagged jets and gluon tagged jets.

Jet Class	<i>udsc</i> quark content	<i>b</i> quark content	gluon content
normal mixture	47.1%	3.8%	48.8%
<i>b</i> tagged jets	17.6%	63.6%	18.7%
gluon tagged jets	10.7%	9.6%	79.6%

Table 7: Compositions of different jet classes in Y events. The statistical errors are less than one per cent.

The use of subtraction techniques which rely only on the knowledge of the proportion of gluon, light, and *b* quark jets populating the three-jet event samples enables a comparison of pure light, *b* quark, and gluon jets.

²There are almost always only two heavy hadrons in an event, because the $g \rightarrow q\bar{q}$ splitting into heavy quarks is strongly suppressed.

³Here the purity is defined as the ratio of real tagged gluons (i.e. jets originating from gluons) to the total number of jets tagged as gluons.

In the following R_g , R_l and R_b are the distributions of any observable for pure gluon jets, for pure light quark jets, and pure b jets, respectively. Then the measured distributions for jets tagged as gluon jets (R_{gtag}) and as b jets (R_{btag}) and in the normal mixture sample (R_{mix}) can be written as follows:

$$\begin{aligned} R_{mix} &= p_{mix}^l \cdot R_l + p_{mix}^b \cdot R_b + p_{mix}^g \cdot R_g \\ R_{btag} &= p_{btag}^l \cdot R_l + p_{btag}^b \cdot R_b + p_{btag}^g \cdot R_g \\ R_{gtag} &= p_{gtag}^l \cdot R_l + p_{gtag}^b \cdot R_b + p_{gtag}^g \cdot R_g \end{aligned} \quad (3)$$

where the p_i^j are the corresponding fractions from Table 7. The data distributions for pure b quark, light quark and gluon jets are then obtained by solving Eq. 3 for R_b , R_l and R_g . The statistical errors on the fractions p_i^j , which are less than one per cent, and their correlations, are fully propagated and included in all error bars shown in the following plots. This has only a small effect on the total errors.

To correct for limited detector acceptance and resolution, a linear acceptance correction factor ($C^{acc} = \frac{R^{MC}}{R^{MC+detector}}$) is also applied to the data in each bin of each distribution. Here R^{MC} denotes the pure simulation and $R^{MC+detector}$ includes the detector simulation.

3 Study of Scale Dependence of the Fragmentation Functions of Quark and Gluon Jets

Jet splittings may be studied with respect to the energy sharing in a splitting process. This analysis is connected to the analysis of the scale dependence (scaling violation) of the fragmentation functions $D_p^H(x_E, s)$ of a parton p into a hadron H described by the DGLAP⁴ equation [15].

For large hadron energy fractions $x_E = E_{hadron}/E_{jet}$ above $\frac{1}{2}$, the lower energy parton in a splitting process cannot contribute. In a $q \rightarrow qg$ splitting process the lower energy parton is almost always the gluon. In addition the splitting kernels corresponding to gluon bremsstrahlung processes diverge for small energy of the emitted gluon. Consequently the non-divergent $g \rightarrow q\bar{q}$ splitting is disfavoured with respect to $g \rightarrow gg$. The (leading order) evolution equations for quarks and gluons therefore simplify to:

$$\frac{dD_g^H(x_E, s)}{d \ln s} = \frac{\alpha_s(s)}{2\pi} \cdot \int_{x_E}^1 \frac{dy}{y} P_{g \rightarrow gg}(y) \cdot D_g^H\left(\frac{x_E}{y}, s\right) \quad (4)$$

$$\frac{dD_q^H(x_E, s)}{d \ln s} = \frac{\alpha_s(s)}{2\pi} \cdot \int_{x_E}^1 \frac{dy}{y} P_{q \rightarrow qg}(y) \cdot D_q^H\left(\frac{x_E}{y}, s\right) \quad (5)$$

where the relevant Altarelli Parisi splitting kernels are:

$$\begin{aligned} P_{q \rightarrow qg}(z) &= C_F \cdot \frac{1+z^2}{1-z} \\ P_{g \rightarrow gg}(z) &= 2C_A \cdot \frac{(1-z(1-z))^2}{z(1-z)} \end{aligned}$$

For a quantitative comparison of gluon and quark fragmentation, it is important to compare the relative size of the observed scaling violation:

$$\mathcal{S}_p = \frac{d \ln D_p^H(x_E, s)}{d \ln s}, \quad (6)$$

⁴Dokshitzer, Gribov, Lipatov, Altarelli and Parisi

where s is the relevant scale. Therefore the following ratio is defined:

$$r_{\mathcal{S}}(x) = \frac{\mathcal{S}_g}{\mathcal{S}_q} = \frac{\frac{d \ln D_g^H(x_E, s)}{d \ln s}}{\frac{d \ln D_q^H(x_E, s)}{d \ln s}}.$$

This ratio can be predicted by solving the DGLAP equation [16]. The limit of $r_{\mathcal{S}}$ as $x_E \rightarrow 1$ is easily calculated:

$$r_{\mathcal{S}}(1) = \lim_{x_E \rightarrow 1} \frac{\frac{d \ln D_g^H(x_E, s)}{d \ln s}}{\frac{d \ln D_q^H(x_E, s)}{d \ln s}} = \frac{C_A}{C_F}$$

Thus $r_{\mathcal{S}}$ can be used directly to determine $\frac{C_A}{C_F}$.

Experimentally $r_{\mathcal{S}}(x_E)$ is accessible by measuring the ratio:

$$r_{\mathcal{S}}(x_E) = \frac{S_g(x_E)}{S_q(x_E)}$$

where

$$S_p(x_E) = \frac{D_p^H(x_E, s_1) - D_p^H(x_E, s_0)}{D_p^H(x_E, s_0)}; \quad p = q, g$$

where s_1 and s_0 correspond to two different energy scales. The division by $d \ln s$ has been omitted here because quark and gluon jets are compared below for the same two scales s_1 and s_0 .

In e^+e^- annihilation, large numbers of gluon jets are available only at Z energies. Therefore the only possibility to access this information is to compare gluon and quark jets obtained from different three-jet topologies like Y- and Mercedes events. A non-trivial problem is the selection of the relevant scales for the corresponding quark and gluon jets. Theoretical studies of hadron production in events with a three-jet topology indicate that a relevant scale is the so-called *hardness* of the process producing the jet [17] which for symmetric topologies is

$$\kappa_{2,3} = E_{2,3} \cdot \sin \frac{\theta_1}{2}$$

where θ_1 is the angle to the nearest other jet, as defined in Fig. 2.

3.1 Results

Sizeable differences have been observed previously between the distributions of the scaled energy x_E of stable hadrons produced in quark jets and in gluon jets [3,22,23]. Figs. 4a and 4b show the scaled energy distributions of charged hadrons in quark and gluon jets measured in the present analysis ⁵.

An approximately exponential decrease of the fragmentation function with increasing x_E is seen, which is more pronounced in the gluon case. The extra suppression at high x_E by almost one order of magnitude of gluon jets relative to quark jets may be expected because, contrary to the quark case, the gluon cannot be present as a valence parton inside the observed hadron. Thus in gluon jets the valence quarks of the hadrons have to be produced in $g \rightarrow q\bar{q}$ splitting processes.

⁵This figure is similar to a figure shown in [3] but now includes also the data collected by DELPHI in 1994.

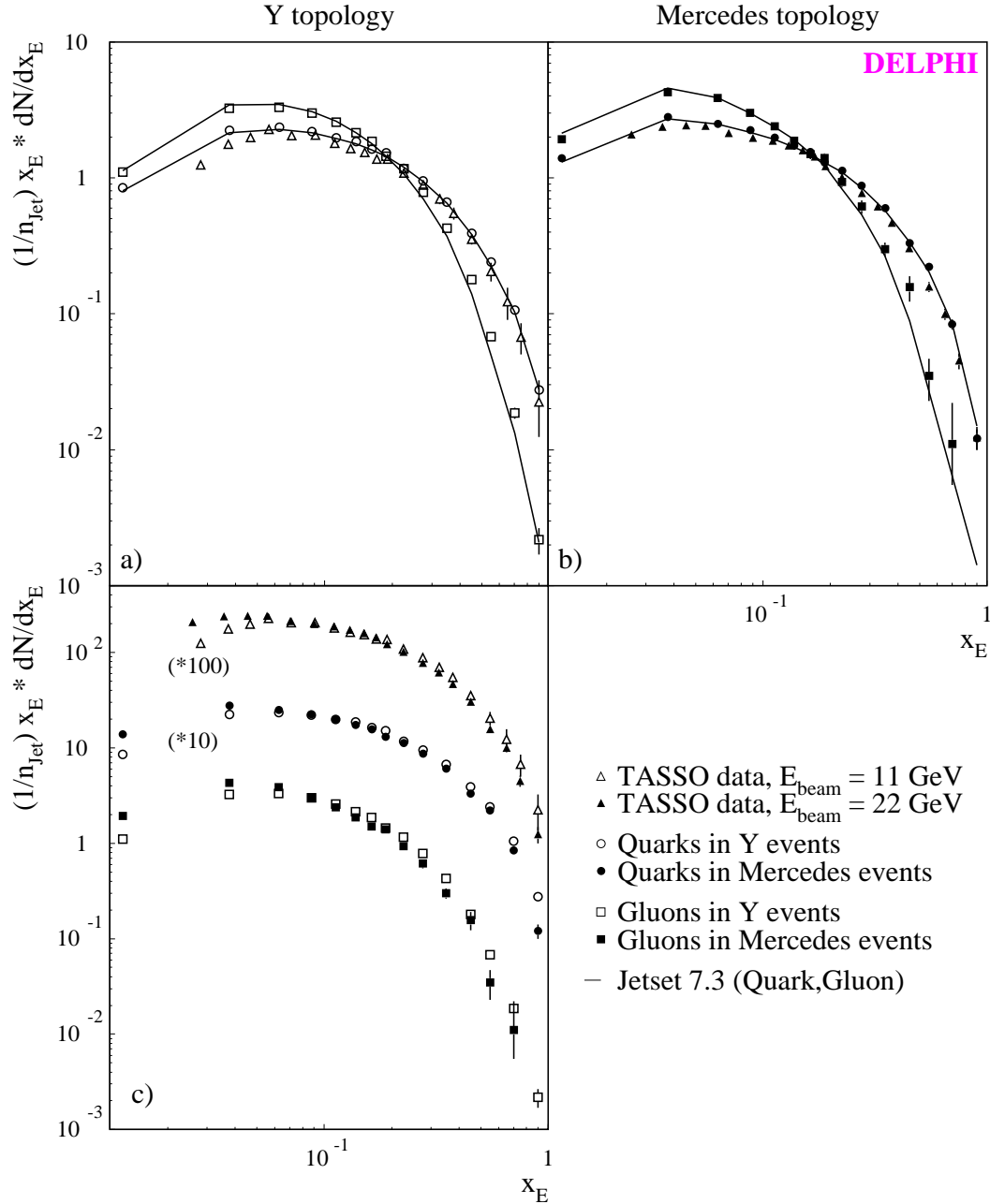


Figure 4: Scaled energy distributions for (a) Y- and (b) Mercedes type events; (c) their comparison at different scales. The solid lines are the corresponding JETSET 7.3 predictions. TASSO data are obtained from all events scaled by $\frac{1}{2}$, because most of the events are two-jet events. All distributions have been multiplied by x_E to focus on the differences at large x_E . The data of this figure will be available at the Durham/RAL HEPDATA database: <http://cpt1.dur.ac.uk:80/HEPDATA>.

The energy spectra and other characteristics of the QCD partonic cascade are expected to depend mainly on the hardness of the corresponding jet [17]. Figs. 4a and 4b also compare the distributions in quark jets in our Mercedes events ($\kappa \approx 26$ GeV) and Y events ($\kappa \approx 12$ GeV) with those in TASSO data at beam energies of 11 and 22 GeV, i.e. with similar hardnesses κ . The quark fragmentation functions in Y- and Mercedes events are seen to be in good agreement with the corresponding TASSO data [24]. The agreement is far less satisfactory if the quark fragmentation function measured from Y- and Mercedes events is compared to the overall e^+e^- data at similar jet energy.

Fig. 4c shows the same data but compares the x_E distributions obtained at different scales; i.e. by TASSO at the two different centre of mass energies [24], from light quark jets in Y- and Mercedes events, and from gluon jets in Y- and Mercedes events. It is observed that the distributions measured from jets in Mercedes events ($\kappa \approx 26$ GeV) show a stronger fall off with hadron energy than those from jets in Y events ($\kappa \approx 12$ GeV). This is similar to the difference in the scaled energy distributions measured by TASSO at the two different centre of mass energies [24].

Fig. 5a compares $S_q(x_E)$ for quark jets in Y- and Mercedes events, i.e. quark jets of $\kappa \approx 12$ GeV and 26 GeV respectively, with the corresponding distributions $S_e(x_E)$ as measured from all events at PETRA at $E_{jet} = \kappa \approx 11$ and 22 GeV [24], i.e. in quark-dominated jets with similar values of κ . The typical pattern expected from scaling violation, a depletion at large energy and an increase at small energy, is observed. The scale dependence vanishes at $x_E \approx 0.1$. The behaviours of S_e and S_q are similar and for large x_E they are consistent within errors. For very small scaled energy x_E , some discrepancies are expected due to the mis-assignment of particles to a jet in three-jet events.

Fig. 5b compares the relative change $S_q(x_E)$ for quark jets with the relative change $S_g(x_E)$ for gluon jets. The typical scaling violation pattern is also observed for gluon jets. It is significantly more pronounced than for quark jets, which is expected owing to the higher gluon splitting probability. The scale dependence again vanishes for $x_E \approx 0.1$. To our knowledge, this is the first direct observation of scaling violations in identified gluon jets and confirms our conjecture in a previous publication [3].

Fig. 5c shows the ratio of the scaling violations in quark and gluon jets, $r_S(x_E) = S_g(x_E)/S_q(x_E)$, which differs from 1 at both small and large x_E . For $x_E \approx 0.1$, $r_S(x_E)$ is undefined experimentally because both S_g and S_q vanish there.

Averaging over $r_S(x_E)$ at large x_E yields

$$\bar{r}_S(0.23 \leq x_E \leq 0.75) = 2.8 \pm 0.8 \pm 0.6$$

where the systematic error quoted is discussed in section 5. Thus at large x_E we observe a large ratio of splitting probabilities in gluon and quark jets, consistent with the expected ratio $r_S(x_E) = C_A/C_F = 9/4$.

Because most hadrons have small x_E , the ratio at small x_E is related to the increase in multiplicity with scale being more pronounced in gluon than in quark jets as observed previously [3]. Due to the stronger scaling violations in gluon jets than in quark jets, the hadron multiplicity in gluon jets increases faster with increasing hardness or energy. Thus scaling violations explain at least in part the observed increase of the multiplicity ratio in gluon and quark jets with energy [3].

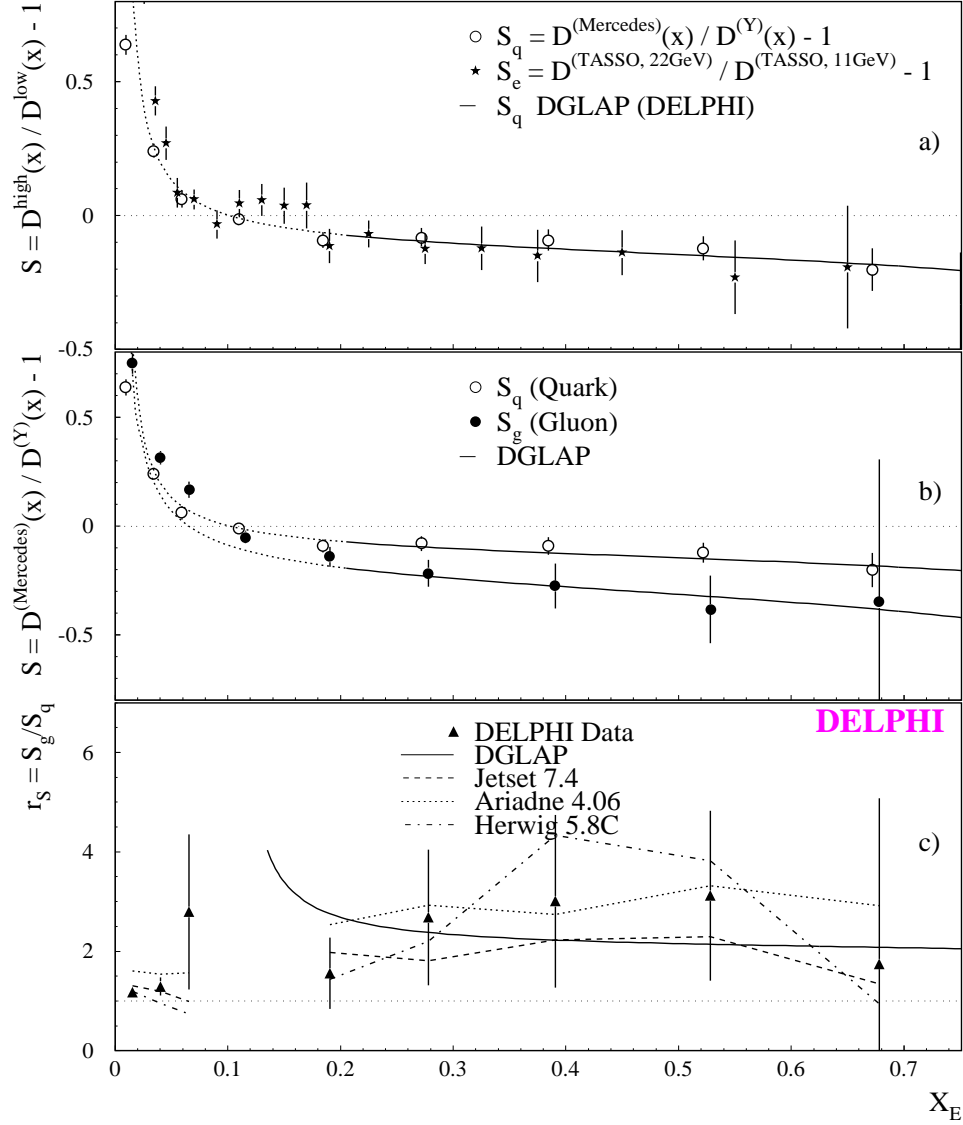


Figure 5: a) The ratio S of quark fragmentation functions at different jet scales. b) Comparison of S_q with S_g . c) The ratio $\frac{S_g}{S_q}$. The solid lines in a)-c) are the expected behaviour as calculated from the DGLAP equation. The dotted parts of the lines in a) and b) correspond to the x_E range not used for parametrizing the quark and gluon fragmentation functions (see Fig. 4) as input for Eq. 5 to obtain these curves.

4 Study of Subjet Splittings

Differences in the splitting properties of quarks and gluons are expected to appear most clearly in the “first” splitting process at large momentum transfer or jet resolution parameter y . To study the splitting of jets into subjets, the jet algorithm used for the subjet definition has been applied only to those particles which have, at the event level, been assigned to the jet under study [8] (see Fig. 6 for an illustration of a subjet). This strategy should result in a more meaningful comparison of the y values of individual jets, as the experimental smearing due to the energy normalization (compare Eq. 1) is smaller.

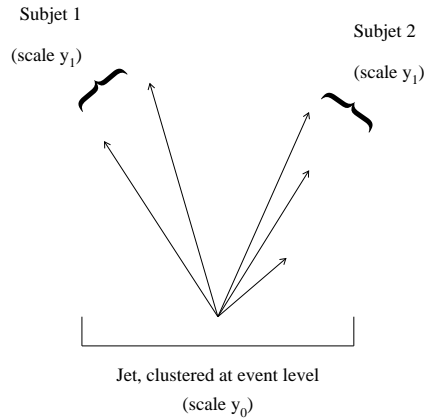


Figure 6: Illustration of a subjet.

The absolute splitting rate of a jet $\Delta N_1(y)$ should be proportional a) to the number of unsplit jets $N_1(y)$ present at a given jet resolution y , b) to some dynamical expression $\mathcal{F}(y)$ containing in particular the coupling constant and the colour factors of the parton initiating the jet, and c) to the size of the y interval Δy , i.e.

$$\Delta N_1(y) = -\mathcal{F}(y) \cdot N_1(y) \cdot \Delta y \quad (7)$$

This expression is analogous to the radiative decay equation with a y dependent decay function $\mathcal{F}(y)$. Thus the *modified differential 1-jet rate* $\tilde{D}_1(y)$, defined as ⁶ :

$$\tilde{D}_1(y) = \frac{1}{N_1(y)} \cdot \frac{\Delta N_1(y)}{\Delta y} = -\mathcal{F}(y),$$

provides a direct measurement of the differential jet decay function $\mathcal{F}(y)$ describing the probability that a jet which has not split so far will split at the scale y . Using the conventional definition of the jet rate:

$$R_1(y) = \frac{N_1(y)}{N_{tot}}$$

where N_{tot} is the initial number of jets and $N_1(y)$ is the number surviving as single jets (“1-jets”) at a fixed y , one obtains:

⁶Following the normal convention, the symbol D is used in this paper for both differential jet rates and for fragmentation functions.

$$\tilde{D}_1(y) = \frac{1}{R_1(y)} \cdot \frac{R_1(y) - R_1(y - \Delta y)}{\Delta y} \approx \frac{d \ln R_1(y)}{dy}$$

Note that this definition has the same formal structure as the scaling violation defined in Eq. 6. A similar approach is used in parton shower simulations [18]. $\tilde{D}_1(y)$ differs from the usual definition of the differential jet rate $D_1(y)$ [19] by the extra factor $1/R_1(y)$. This definition can be generalized also to higher rank (second, third, ...) splittings, yielding for the n^{th} splitting:

$$\tilde{D}_n(y) = \frac{1}{R_n(y)} \cdot \frac{R_n(y) - R_n(y - \Delta y)}{\Delta y} + \frac{R_{n-1}(y)}{R_n(y)} \cdot \tilde{D}_{n-1}(y)$$

Here the (sub-) jet rates $R_n(y)$ are defined as usual by $R_n = N_n(y)/N_{tot}$, where $N_n(y)$ is the number of jets in which $n - 1$ splittings occurred up to the given jet resolution y . The differential jet rates $D_n(y)$ measured at different values of y are by construction uncorrelated, in contrast to the jet rates R_n or the average subjet multiplicities. The subjet multiplicity $N(y)$ follows from the weighted mean of the jet rates:

$$N(y) = \sum_{n=1}^{\infty} n R_n(y) \quad (8)$$

For very small y , it converges to the hadron multiplicity.

The decay functions Γ corresponding to the splittings shown in Fig. 1, which can be identified with the decay function $\mathcal{F}(y)$ defined above and thus with the differential jet rates $\tilde{D}_1(y)$, and the corresponding Sudakov form factors $\Delta_{q,g}$, which can be identified with the 1-jet rates $R_1^{q,g}$, have been calculated in the NLLA ⁷ for the Durham algorithm [20]:

$$\begin{aligned} \Gamma_{g \rightarrow gg}(Q, q) &= \frac{2C_A \alpha_s(q)}{\pi q} \left(\ln \frac{Q}{q} - \frac{11}{12} \right) \\ \Gamma_{g \rightarrow q\bar{q}}(Q, q) &= \frac{2n_F T_F \alpha_s(q)}{3\pi q} \\ \Gamma_{q \rightarrow qg}(Q, q) &= \frac{2C_F \alpha_s(q)}{\pi q} \left(\ln \frac{Q}{q} - \frac{3}{4} \right), \end{aligned}$$

where Q in [20] is the centre of mass energy of the jet production process to be identified with the scale κ in this paper, $q = \kappa \cdot \sqrt{y}$, and

$$\tilde{D}_1^g = \Gamma_{g \rightarrow gg} + \Gamma_{g \rightarrow q\bar{q}} \quad (9)$$

$$\tilde{D}_1^q = \Gamma_{q \rightarrow qg}. \quad (10)$$

The 1-jet rates are then given by:

$$\begin{aligned} R_1^g = \Delta_g(Q) &= \exp \left(- \int_{Q_0}^Q dq (\Gamma_{g \rightarrow gg} + \Gamma_{g \rightarrow q\bar{q}}) \right) \\ R_1^q = \Delta_q(Q) &= \exp \left(- \int_{Q_0}^Q dq (\Gamma_{q \rightarrow qg}) \right) \end{aligned}$$

and the ratio of the gluon to quark splitting functions mainly depends on the colour factor ratio C_A/C_F [21]:

⁷Next to Leading Log Approximation

$$\tilde{r}_1(y) = \frac{\tilde{D}_1^g}{\tilde{D}_1^q} = \frac{\Gamma_{g \rightarrow gg} + \Gamma_{g \rightarrow q\bar{q}}}{\Gamma_{q \rightarrow qq}} = \frac{C_A}{C_F} \cdot \frac{\ln y + \left(\frac{11}{6} - \frac{2n_F T_F}{3C_A}\right)}{\ln y + \frac{3}{2}}. \quad (11)$$

For $n_F = 3$ this yields $\tilde{r}_1(y) \equiv \frac{C_A}{C_F}$, independent of y .

Eq. 11 may be compared with the naïve expectation:

$$\tilde{r}_1 = \frac{C_A + \eta n_F T_F}{C_F} \quad (12)$$

where the term $\eta n_F T_F$ ($0 \leq \eta \leq 1$) accounts for the non-divergent contribution of the $g \rightarrow q\bar{q}$ splitting. Due to the large c and b quark masses, the value of n_F is energy dependent. For Y events, the JETSET model predicts $n_u : n_d : n_s : n_c : n_b = 1 : 1 : 1 : 0.74 : 0.086$ for the first gluon splitting, which corresponds to $n_F \simeq 3.83$, whereas in the low energy limit $n_F \simeq 3$. Here η denotes the extra suppression factor of the $g \rightarrow q\bar{q}$ splitting compared with $g \rightarrow gg$. Numerically, allowing the full range for η , from 0 to 1, one expects $\tilde{r}_1 = 2.25 - 3.7$.

4.1 Results

The jet rates $R_n(y)$, the differential jet rates $D_n(y)$, and the modified differential jet rates $\tilde{D}_n(y)$ have been measured for quarks and gluons in Y- and Mercedes events. The results for both event types are consistent. Because of their better statistical precision, only the results obtained from Y events are presented.

The measured values of R_1 , $y_1 D_1$, and $y_1 \tilde{D}_1$ for quark and gluon jets, and of the ratio $\tilde{r}_1 = \tilde{D}_1^g / \tilde{D}_1^q$, are compared with the NLLA calculation [21] in Figs. 7(a-d), $y_1 \tilde{D}_1$ and \tilde{r}_1 are also compared with the predictions of fragmentation models in Figs. 7(e-f).

All of the fragmentation models considered describe the observed behaviour of \tilde{D}_1 and \tilde{r}_1 reasonably well. The NLLA calculation⁸ provides at least a qualitative description of the behaviour of R_1 , D_1 , and \tilde{D}_1 for not too small y_1 . In particular, the differences between quarks and gluons are correctly represented. Some differences between the calculations and the measurements should be expected as no fragmentation effects are taken into account⁹. A good description of $\tilde{D}_1^q(y)$ and $\tilde{D}_1^g(y)$ is most important, as these quantities directly measure the splitting kernels for quarks and gluons, which are basic predictions of QCD.

ratio	Y events		Mercedes events		NLLA
	data	Jetset	data	Jetset	calculation
\tilde{r}_1^{max}	$2.77 \pm 0.11 \pm 0.10$	2.94 ± 0.05	$2.44 \pm 0.20 \pm 0.15$	2.72 ± 0.08	2.67

Table 8: Ratio of the modified differential one jet-rate for Y- and Mercedes events (data and simulation) at the maximum, $0.018 \leq y_1 \leq 0.100$. For the NLLA calculation $n_F = 5$ is used.

In the range $0.018 \leq y \leq 0.100$, the ratio \tilde{r}_1 is $2.77 \pm 0.11 \pm 0.10$ (see Fig. 7d and Table 8), where the systematic error is discussed in detail in section 5. The fragmentation

⁸ Λ_{QCD} has been set to 300 MeV.

⁹ Hadronization corrections cannot be calculated easily as the number of splittings in a parton shower simulation is relatively small. Consequently, in an important fraction of the events, the primary parton of a jet does not split at all.

models agree well with the data. ARIADNE [25] is slightly higher in the region of the maximum. This is understood as being due to a higher $g \rightarrow q\bar{q}$ contribution in ARIADNE. Studies with the JETSET model indicate that the fall off of \tilde{r}_1 at very large y is due to the absence of the $g \rightarrow q\bar{q}$ contribution in this y range. This influence may also be indicated by the NLLA calculation in Fig. 7d. However, it is to be noted that the LLA implies a small angle approximation, thus it may be invalid at large y towards the limit of resolved jets.

At small y , below about 10^{-2} , the NLLA prediction starts to deviate from the observed \tilde{D}_1^g , and for slightly smaller y also from \tilde{D}_1^q . At small y ($\kappa \cdot \sqrt{y} \sim \mathcal{O}(1\text{GeV})$), fragmentation effects are expected to set in. It is important to realize that these effects start to be important at larger values of y , that is at larger effective masses ($m \propto \kappa \cdot \sqrt{y}$), for gluons than for quarks. This may be again because quarks are valence particles of the hadrons whereas gluons are not, so that at least one additional $g \rightarrow q\bar{q}$ splitting has to occur in gluon fragmentation.

The indication of this additional g splitting appears most clearly from the strong suppression of the gluon fragmentation function compared to the quark fragmentation function (compare Fig. 5) at large x_E . It also has a direct effect on the evolution of the experimental splitting functions \tilde{D}_1 at small y . In fact \tilde{D}_1^g rises far less rapidly with falling y than expected. For y less than about 10^{-3} , where also \tilde{D}_1^q already deviates from the NLLA expectation, \tilde{D}_1^g appears to be even greater than \tilde{D}_1^q . This directly implies that in this y range more quarks split than gluons. This is even amplified by the fact that more unsplit quarks are present at such y values (compare Fig. 7a). This behaviour, which may be induced by differences between quark and gluon fragmentation due to the valence structure of the hadrons, is opposite to the naïve expectation for the splitting behaviour of quarks and gluons due to the colour factors. This has important consequences for the evolution of gluon and quark jets, and especially for the hadron multiplicity in quark and gluon jets, as is discussed below. It is instructive, however, first to study the higher rank splittings.

Fig. 8 shows $y\tilde{D}_n(y)$, $yD_n(y)$ and $R_n(y)$ for the $n = 1^{st}$ to the $n = 4^{th}$ splitting. It is evident that differences in $\tilde{D}(y)$ start to vanish with higher splitting rank. This is most clearly seen in the ratio \tilde{r}_n (Fig. 9) which is almost unity for $n \geq 4$. This is understood because of the sizeable number of gluons in both types of jets. The only difference remaining is the initial quark. In other words, each jet is predominantly a “gluon jet”. The higher splitting probability in quark jets at low y together with the higher fraction of unsplit quark jets compensate the initially higher subjet rate D_1 in gluon jets (see also r_1 in Fig. 9). This mechanism also holds for the higher jet rates D_2 to D_4 , contrary to the behaviour of the \tilde{D}_n distributions, and is again most clearly seen in the corresponding ratios (see Fig. 9). The difference of the behaviour of the \tilde{D}_n and D_n distributions is due to the different number of quark and gluon initiated jets (with n subjets) present at a given y which are able to split into $n + 1$ subjets.

From this discussion, the behaviour of the subjet multiplicity and, in the limit of small y , the hadron multiplicity in quark and gluon jets is also understood. Fig. 10a shows the average subjet multiplicity minus one as a function of y . The subtraction of 1 accounts for the presence of the initial quark or gluon. A similar result was presented in [26]. Initially, at large y , the multiplicity rises faster with falling y for gluons than for quarks. The gluon to quark ratio (Fig. 10b) reaches values around two: the maximum ratio of the subjet multiplicity distributions of gluon and quark jets, r_M^{max} , is measured to be $2.03 \pm 0.15 \pm 0.12$ for Y events and $1.67 \pm 0.23 \pm 0.13$ for Mercedes events for $y \sim 0.016$ (mean for $-2.0 < \lg(y) < -1.5$). These systematic errors are discussed in detail in

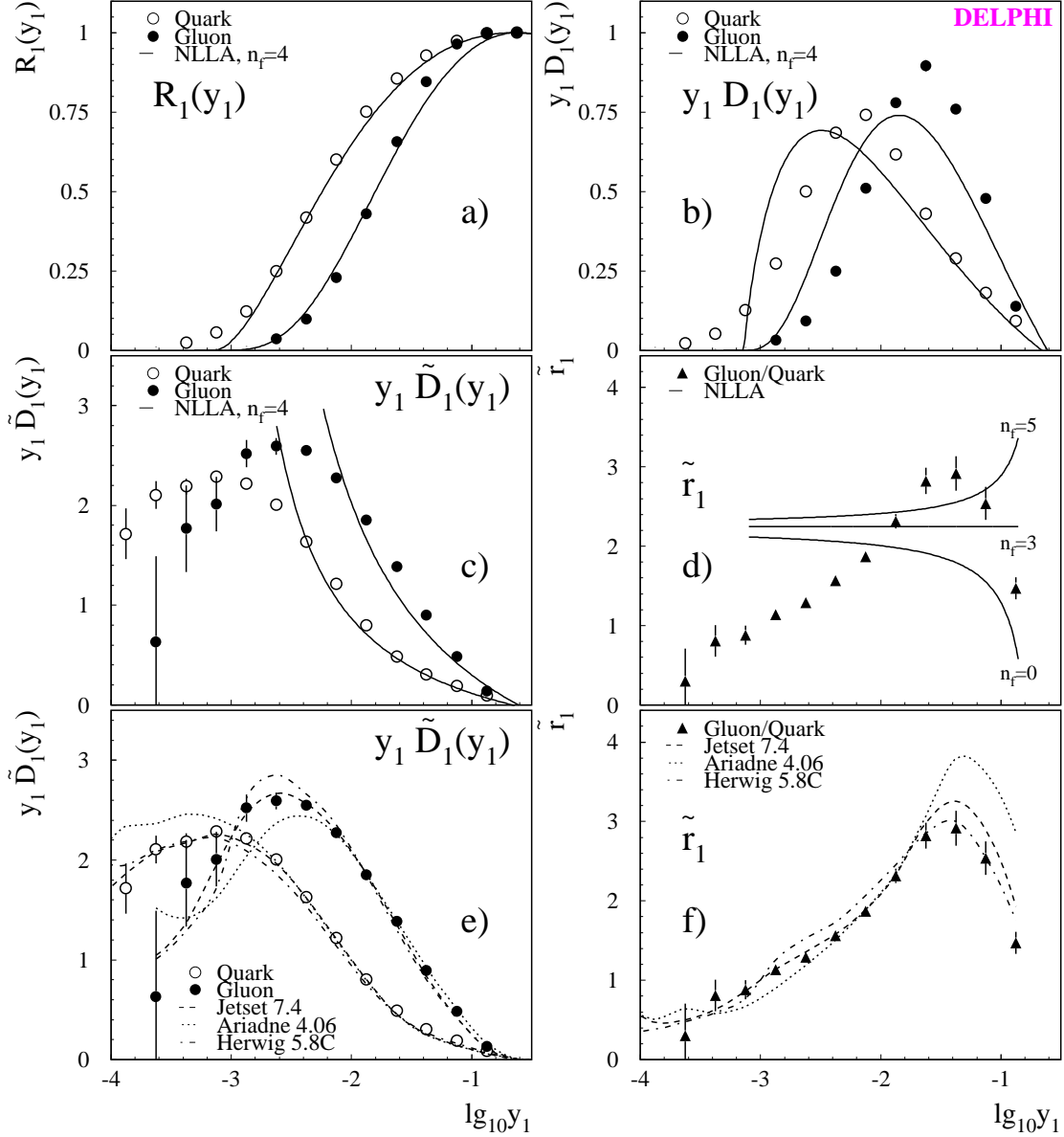


Figure 7: Subject rates in Y events: *a*) shows the total jet rates R_1 for quark and gluon jets; *b*) shows the differential jet rates D_1 multiplied by $y_1 \cdot \ln(10)$, which can be rewritten as $dR_1(\lg_{10} y_1)/d \lg_{10} y_1$ and has the advantage that the very strong increase of the distributions is prevented; *c*) shows the splitting functions \tilde{D}_1 similarly multiplied by $y_1 \cdot \ln(10)$; *d*) shows the ratio $\tilde{r}_1 = \tilde{D}_1^g/D_1^g$. The curves in *a*) to *d*) show the NLLA prediction. In *e*) and *f*) the data are the same as in *c*) and *d*), but the curves show the predictions from simulations with JETSET, ARIADNE, and HERWIG tuned to DELPHI data. The data of this figure will be available at the Durham/RAL HEPDATA database: <http://cpt1.dur.ac.uk:80/HEPDATA> .

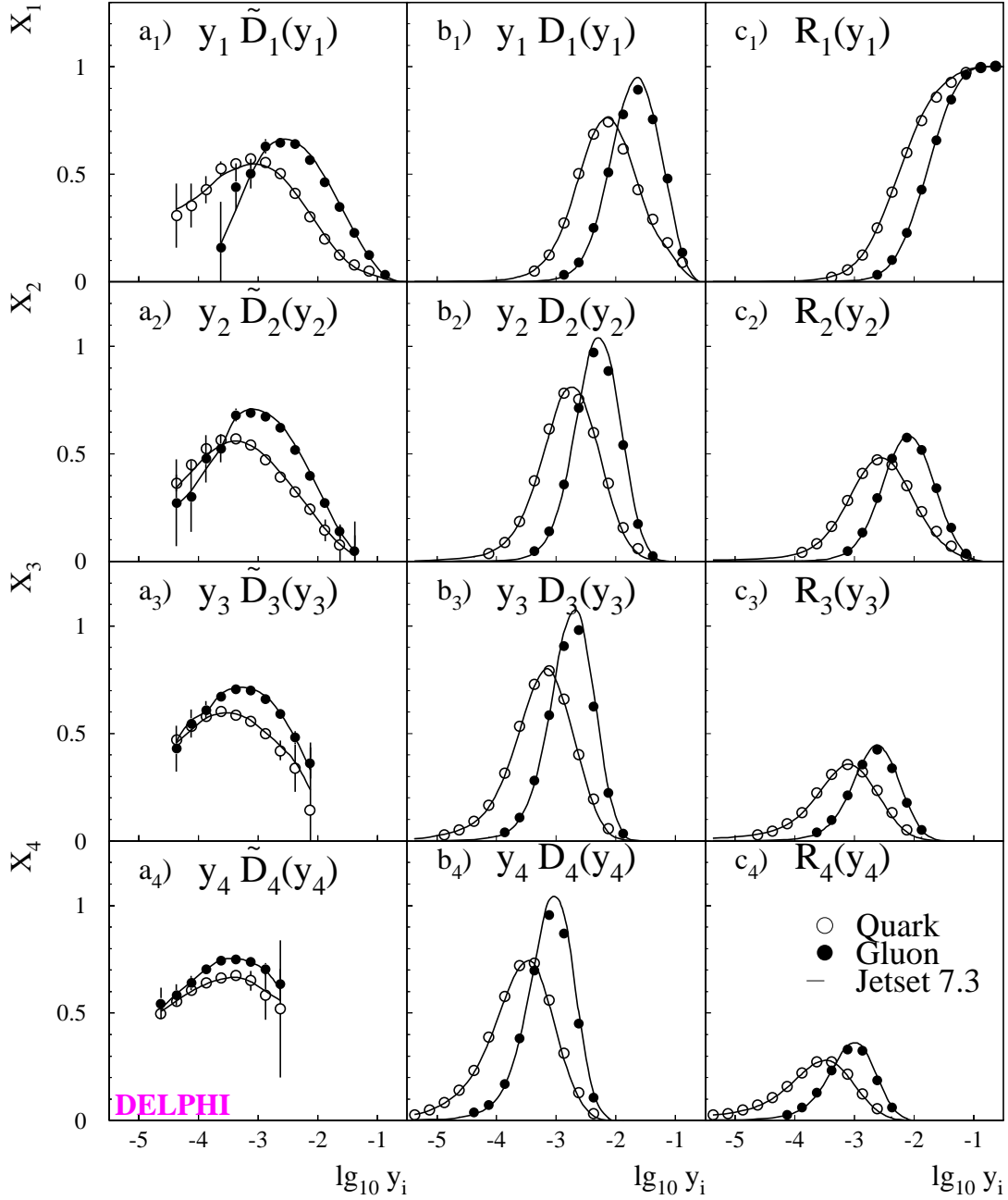


Figure 8: Subjet rates in Y events. c_1) to c_4) show the total jet rates R_1 to R_4 for quark and gluon jets with the prediction of JETSET superimposed. b_1) to b_4) show the differential jet rates D_i multiplied by $y_i \cdot \ln(10)$. a_1) to a_4) show the splitting functions \tilde{D}_i multiplied by $\frac{1}{4}y_i \cdot \ln(10)$. The factor $y_i \cdot \ln(10)$ results from the same factor in the D_i distributions while the additional factor $\frac{1}{4}$ results from the bin width $\Delta \lg_{10}(y_i)$ by which \tilde{D}_i has not been divided. Therefore, \tilde{D}_i is directly $\Delta N_i/N_i$ as defined in Eq. 7 yielding the fraction of jets splitting in a given interval $\Delta \lg_{10}(y_i)$ with respect to the number of jets available for the splitting from i to $(i + 1)$ subjets.

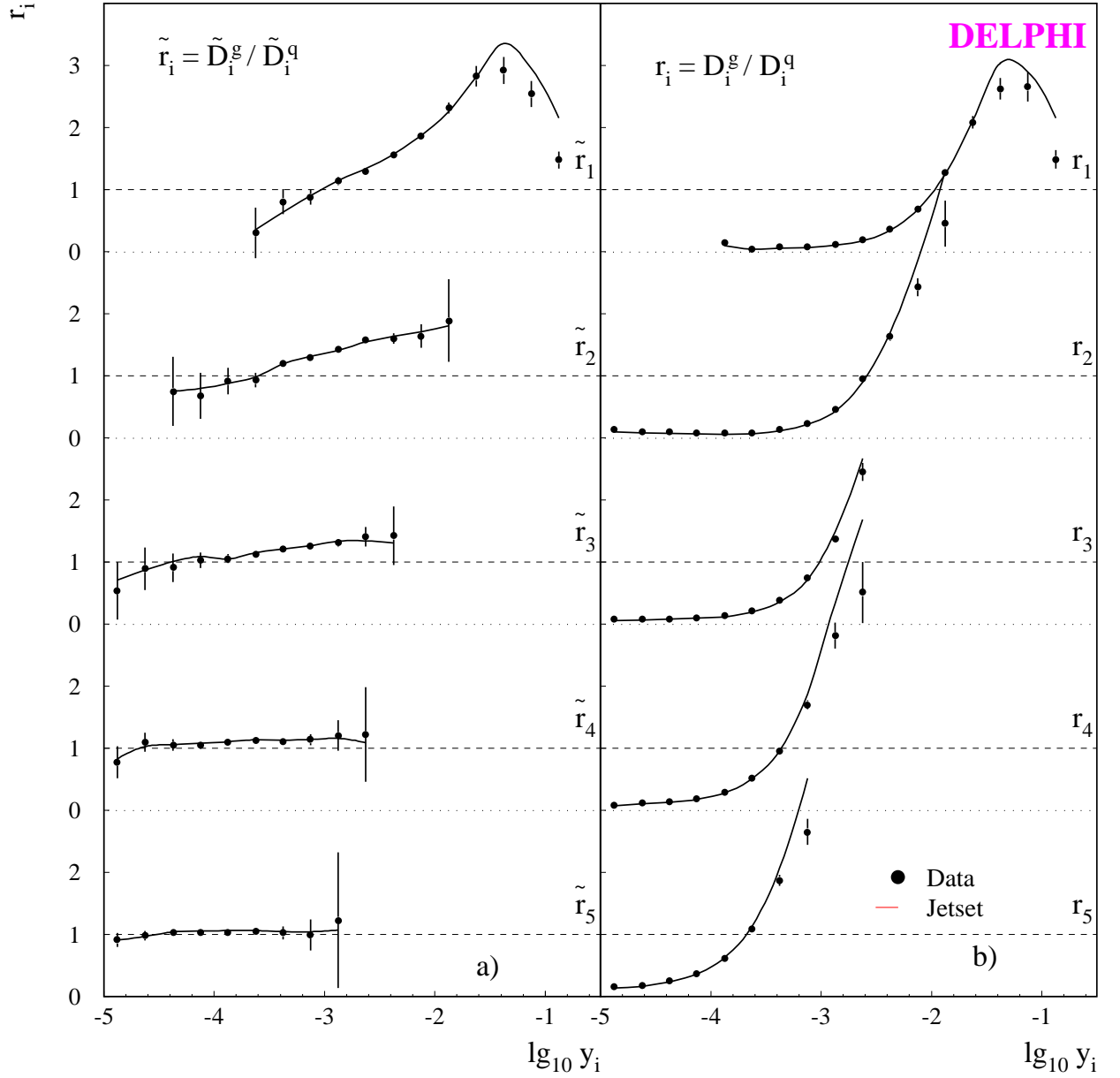


Figure 9: Ratios of the modified differential subjet rates ($\tilde{r}_i = \tilde{D}_i^g / \tilde{D}_i^q$) and the differential subjet rates ($r_i = D_i^g / D_i^q$) in Y events. The curves show the expectations from JETSET.

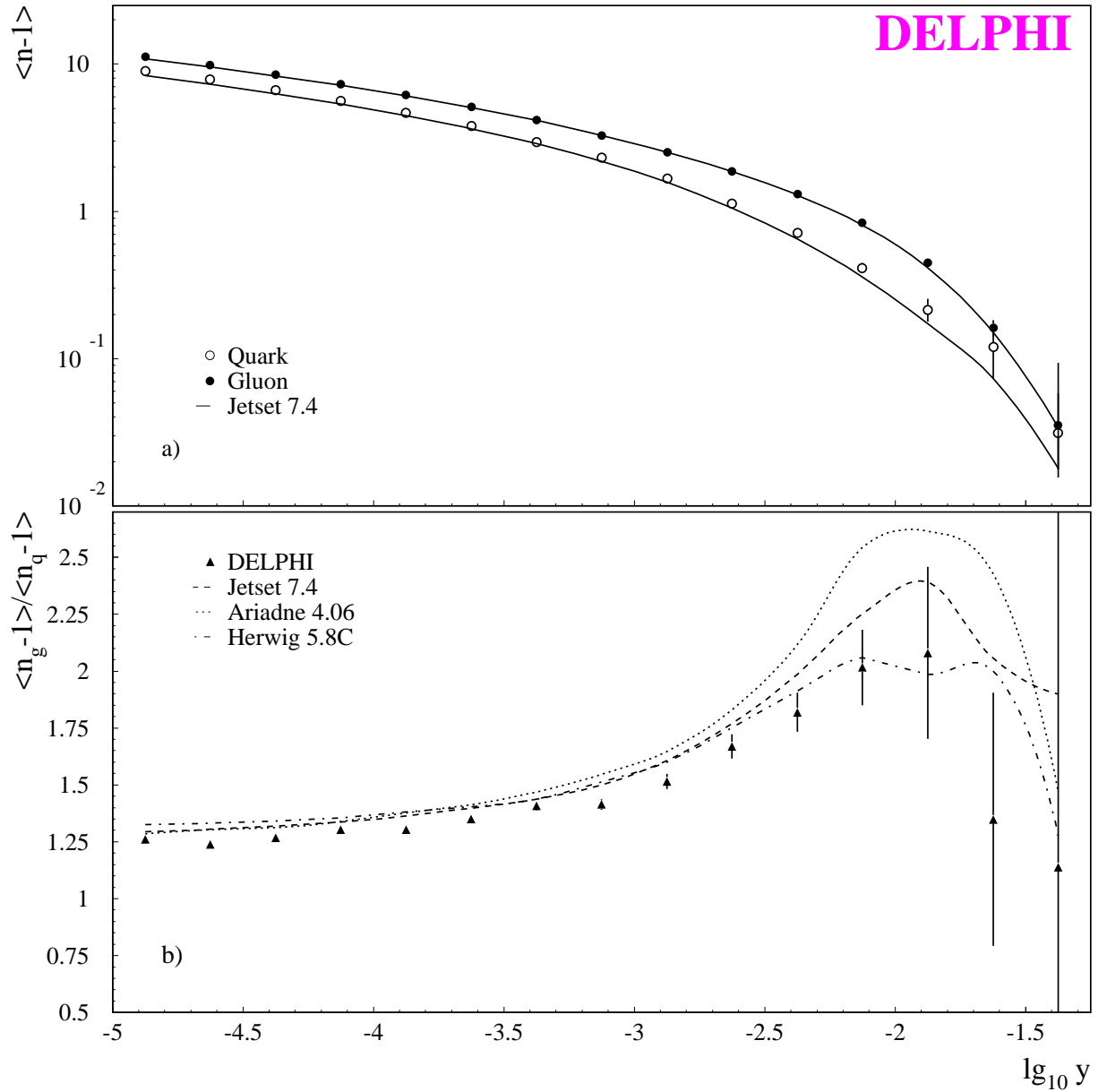


Figure 10: a) Subjet multiplicity minus one in quark and gluon jets in Y events; b) Ratio of quark subjet multiplicity minus one to gluon subjet multiplicity minus one in Y events. The curves show the expectations from the JETSET, ARIADNE and HERWIG models. The data of this figure will be available at the Durham/RAL HEPDATA database: <http://cpt1.dur.ac.uk:80/HEPDATA> .

section 5. The ratio falls off for smaller y and rapidly converges to the stable hadron multiplicity ratio, $r_M^{Had} = 1.26 \pm 0.01$ (the systematic error is negligible). The fall off of the multiplicity ratio coincidences with the deviation \tilde{D}_1^g from the QCD expectation (compare Fig. 7) and the correspondingly reduced gluon to quark splitting rate ratio.

5 Systematics

The emphasis of this paper is on the qualitative measurement of several distributions to obtain as complete as possible an idea of the differences between quark and gluon splitting and fragmentation. As well as quoting the systematic uncertainties on the defined values \tilde{r}_1^{max} , \bar{r}_S , r_M^{max} and r_M^{Had} , the effect of the most important sources of systematic uncertainty on the complete distributions is therefore also discussed.

To compare distributions obtained with different parameters, we use the variable

$$\langle \chi^2/n \rangle = \frac{1}{n_{bin}} \sum_{bins \text{ with } \sigma_X/X < 50\%} \frac{(X_{Ref} - X_{Sys})^2}{\sigma_X^2}$$

where n_{bin} is the number of bins in which the relative error of the reference sample (usually the histogram of the distribution) does not exceed 50%, X_{Ref} is the bin content of the reference sample, and X_{Sys} is the content of a sample obtained with varied cuts. Finally a qualitative check of the most relevant results of the analysis has been performed using alternative jet algorithms.

The following sources of systematic uncertainties have been studied:

1. Variation of gluon purities in terms of varying P_E and P_J

The cut on the event probability to take an event as a b-quark event has been varied from $-\lg_{10} P_E = 1.25$ to 1.75 and simultaneously the cut on the probability to identify a jet as a b-quark jet in the range $-\lg_{10} P_J = 0.75 \dots 1.25$. This corresponds to a variation of the gluon purity. $\langle \chi^2/n \rangle$ is found to be below 50% without any significant systematic shift in any variable.

2. Variation of the cut on the minimal particle momentum

The cut on the minimal particle momentum has been decreased from 400 MeV/c to 200 MeV/c. $\langle \chi^2/n \rangle$ turns out to be lower than 75%. The distributions of D_1 and R_1 show a small systematic shift from small y_1 to medium y_1 which results from a discrepancy between measured data and the detector simulation. This effect is the same in quark and gluon jets and cancels in the ratios. The x_E distributions show a tiny enhancement in the first bin which cancels in the S distribution. For all fragmentation functions, $\langle \chi^2/n \rangle$ is below 50%.

3. Variation of y_{cut}

Three-jet events have been selected using $y_{cut}=0.01$ and $y_{cut}=0.02$ instead of $y_{cut}=0.015$. A very large $y_{cut}=0.1$ has also been tried but leads to an unacceptably large bias of the geometry, especially for the Y events.

Using $y_{cut}=0.01$ shifts the D_1 distributions to lower y . For $y_{cut}=0.02$, more jets split at larger y . The resulting effect on the D_1 distribution is smaller than 2% in each bin. It cancels completely in the distributions of \tilde{D}_1 for both quark and gluon jets. If symmetric three-jet events are selected by cutting only on the event geometry but not on y_{cut} , i.e. by forcing all events to a three-jet topology and then applying the angle cuts in section 2.4, a shift of about 1% in D_1 to larger y_1 of about 1% for both quark and gluon jets in Y events is observed which nearly cancels in all ratios (\tilde{D}_i ,

\tilde{r}_i , and r_i). In Mercedes events, this shift becomes larger, about 5%. The $\langle \chi^2/n \rangle$ is below 25% for the \tilde{r}_i distributions.

Cutting on $y_{cut}=0.02$ or omitting this cut results in a softer fragmentation in both quark and gluon jets while choosing $y_{cut}=0.01$ makes the fragmentation harder. This effect is about $\pm 2\%$. The deviation is larger for quarks (-5%) when omitting this cut. Consequently, S_q is about 20% higher without this cut than for the reference sample with $y_{cut}=0.015$ for large x_E .

4. Modification of the acceptance correction

Selecting only events at the generator level which satisfy the criteria for symmetric events for both simulated and detector level, one finds that the D_i distributions become narrower for both quark and gluon jets. The maxima of the \tilde{D}_i distributions are slightly shifted to smaller y . This effect is nearly the same for quark and gluon jets and cancels in the ratio \tilde{r}_i . Here $\langle \chi^2/n \rangle$ is 40% for \tilde{r}_1 and lower than 10% for the higher rank splittings. The fragmentation functions are not affected by this modification.

Source	\bar{r}_S	\tilde{r}_1^{max}	r_M^{max}	r_M^{Had}
	Y events			
1. Gluon purities	± 0.28	± 0.03	± 0.04	± 0.00
2. p_{min}	± 0.48	± 0.09	± 0.10	± 0.00
3. y_{cut}	± 0.29	± 0.02	± 0.06	± 0.00
4. Acc. correction	± 0.20	± 0.03	± 0.02	± 0.00
total	± 0.65	± 0.10	± 0.12	± 0.00
	Mercedes events			
1. Gluon purities		± 0.06	± 0.06	± 0.01
2. p_{min}		± 0.12	± 0.10	± 0.01
3. y_{cut}		± 0.06	± 0.06	± 0.01
4. Acc. correction		± 0.03	± 0.02	± 0.00
total		± 0.15	± 0.13	± 0.02

Table 9: Systematic uncertainties on \bar{r}_S , \tilde{r}_1^{max} , r_M^{max} , and r_M^{Had}

The above sources of uncertainties lead to the systematic errors on the values \bar{r}_S , \tilde{r}_1^{max} , r_M^{max} , and r_M^{Had} listed in Table 9. These values have been obtained as half the difference between the reference sample and the samples with the varied cuts. The overall systematic error is then assigned to the quadratic sum of the four individual contributions. This is a conservative estimation due to the correlations between the samples. As \bar{r}_S is obtained from both Y- and Mercedes events, the corresponding errors are quoted only once.

As alternatives to the k_T cluster algorithm, the Jade [27] ($E0$ -scheme) and the Geneva [28] algorithms have been used to cluster the event and the jets. This investigation is to be seen as a qualitative analysis as the y_{cut} values chosen to select three-jet events ($y_{cut}=0.04$ for Jade and $y_{cut}=0.05$ for Geneva) have not been explicitly optimized for the three-jet statistics or for good agreement of the parton and hadron level three-jet rates.

The observation of the splitting functions and jet rates are not directly comparable as the y values differ for the jet algorithms. For all jet algorithms, a significant peak in the r_1 distribution at large y is visible, as well as the decrease for small y . The ratio of the higher rank (3,4,...) splitting functions tend to be 1 for both the Jade and Geneva algorithms. The result for the subjet multiplicities is similar to the k_\perp case.

The fragmentation functions depend on the cluster algorithm as well. Jade tends to produce a softer energy spectrum than the k_\perp algorithm, whereas the fragmentation is measured to be harder when using Geneva.

r_S is measured to be $\approx 5\%$ larger when events and jets are clustered with Jade, but the errors are increased compared to the k_\perp case due to the softer fragmentation.

6 Conclusions

Light quark and gluon jets of similar energy have been selected from planar symmetric three-jet events measured with DELPHI at LEP. Gluon jets have been selected in heavy quark events using an impact parameter technique and heavy quark contributions have been depleted in a mixed quark/gluon jet sample. Properties of pure quark and gluon jets have been obtained by a subtraction method.

Jet splitting has been studied using the scale dependence of the quark and gluon fragmentation functions. Y- and Mercedes events provide sources of quark and gluon jets at different energy scales. The scale dependence of the fragmentation function measured in quark jets shows the typical scaling violation pattern as observed in the TASSO events at different centre-of-mass energies. For the first time, scaling violations have also been observed in identified gluon jets. At large hadron energies, the ratio of the scaling violations in quark and gluon jets, i.e. the ratio of the relative changes in the fragmentation functions for quarks and gluons, is measured to be:

$$r_S(0.23 \leq x_E \leq 0.75) = 2.8 \pm 0.8 \pm 0.6$$

This value is comparable with the QCD expectation $r_S(x_E \rightarrow 1) = C_A/C_F = 9/4$ and confirms that the ratio of gluon to quark splitting can be explained mainly by the colour factors. The scale dependence of the ratio of the hadron multiplicities in quark and gluon jets is due at least in part to the observed scaling violations.

This finding has been confirmed by studying the differential subjet splittings $\tilde{D}_p(y)$. The maximum of the ratio of the first splitting in quark and gluon jets is measured to be:

$$\tilde{r}_1^{max} = 2.77 \pm 0.11 \pm 0.10$$

This result is slightly bigger than the naïve expectation C_A/C_F or the expectation from an NLLA QCD calculation ($2.25 \rightarrow 2.67$ for $n_F = 3 \rightarrow 5$), but is in good agreement with the predictions of fragmentation models.

It is found that fragmentation effects set in at higher y (this implies that they set in at a higher mass as $m \propto \kappa \cdot \sqrt{y}$) for gluons than for quarks. Theoretical calculations should therefore be evolved to a lower y cutoff for quarks than for gluons when comparing directly to data.

Finally, the study of higher rank splittings in quark and gluon jets leads to the conclusion that the initially higher subjet multiplicity in gluon jets is compensated at smaller y already due to the larger differential splitting rate D_1^q in quark jets. In the limit of small y , this explains the relatively small multiplicity ratio between gluon and quark jets, although the primary splittings of quarks and gluons follow the QCD colour factor expectation, as the measurements of r_D and \tilde{r}_D demonstrate.

Acknowledgements

We are greatly indebted to our technical collaborators and to the funding agencies for their support in building and operating the DELPHI detector, and to the members of the CERN-SL Division for the excellent performance of the LEP collider. We also thank Yu.L. Dokshitzer, T. Sjöstrand, S. Catani and P. Kroll for useful and illuminating discussions.

References

- [1] S.J. Brodsky, J. Gunion, Phys. Rev. Lett. **37** (1976) 402;
K. Konishi, A. Ukawa, G. Veneziano, Phys. Lett. **B78** (1978) 243.
- [2] A.H. Mueller, Nucl. Phys. **B241** (1984) 109;
J.B. Gaffney, A.H. Mueller, Nucl. Phys. **B250** (1985) 109;
E.D. Malaza, B.R. Webber, Phys. Lett. **B149** (1984) 501;
E.D. Malaza, Zeit. Phys. **C31** (1986) 143;
I.M. Dremin, R.C. Hwa, Phys. Lett. **B324** (1994) 477;
I.M. Dremin, V.A. Nechitailo, Modern Phys. Lett. **A9** (1994) 1471.
- [3] DELPHI Collaboration, Z. Phys. **C70** (1996) 179.
- [4] OPAL Collaboration, Z. Phys. **C58** (1993) 387;
OPAL Collaboration, Z. Phys. **C68** (1995) 179;
ALEPH Collaboration, Phys. Lett. **B313** (1993) 535;
ALEPH Collaboration, Phys. Lett. **B384** (1996) 353.
- [5] CLEO Collaboration, Phys. Rev. **D56** (1997) 17;
OPAL Collaboration, Phys. Lett. **B388** (1996) 659;
for a compilation see:
J. Fuster et al., Proc. of QCD 96, S. Narison ed., Nucl. Phys. **B54A** (Proc. suppl.) (1997);
ALEPH Collaboration, Z. Phys. **C76** (1997) 191.
- [6] DELPHI Collaboration, Nucl. Instr. and Meth. **A303** (1991) 233.
- [7] DELPHI Collaboration, Nucl. Inst. and Meth. **A378** (1996) 57.
- [8] O. Klapp, Diplomarbeit *Quark- und Gluon-jets aus Z-Zerfällen — Vergleichende Studien des Jetendzustandes und der Substruktur*, WU D 95-15 (University of Wuppertal, Germany).
- [9] S. Catani, Yu.L. Dokshitzer, M. Olsson, G. Turnrock, B.R. Webber, Phys. Lett. **B269** (1991) 432;
S. Bethke, Z. Kunszt, D.E. Soper, W.J. Stirling, Nuclear Physics **B370** (1992) 310.
- [10] G. Borisov and C. Mariotti, Nucl. Inst. and Meth. **A372** (1996) 181.
- [11] T. Sjöstrand, Comp. Phys. Comm. **39** (1986) 346;
T. Sjöstrand, M. Bengtsson, Comp. Phys. Comm. **43** (1987) 367;
T. Sjöstrand, *JETSET 7.3 Program and Manual*, CERN-TH 6488/92.
- [12] DELPHI Collaboration, Z. Phys. **C73** (1996) 11.
- [13] DELPHI Collaboration, *DELPHI event generation and detector simulation*, DELPHI 89-67 PROG-142.
- [14] G. Marchesini, B.R. Webber, Nucl. Phys. **B283** (1984) 1;
B.R. Webber, Nucl. Phys. **B283** (1984) 492.
- [15] V.N. Gribov, L.N. Lipatov, Sov. J. Nucl. Phys. **15** (1972) 438 and 675;
G. Altarelli, G. Parisi, Nucl. Phys. **B126** (1977) 298;
Yu.L. Dokshitzer, Sov. Phys. JETP **46** (1977) 641.
- [16] P. Nason, B.R. Webber, Nucl. Phys. **B421** (1994) 473.
- [17] Yu.L. Dokshitzer, private communication;
Yu.L. Dokshitzer, V.A. Khoze, A.H. Mueller, S.I. Troyan, *Basics of perturbative QCD*, Editions Frontieres, 1991, chapter 1 and 9;
Yu.L. Dokshitzer, S.I. Troyan, V.A. Khoze, Sov. J. Nucl. Phys. **47** No.5 (1988) 1384.
- [18] T. Sjöstrand, Phys. Lett. **B157** (1985) 321.
- [19] L. Smolik, PhD thesis, Heidelberg (1990), DESY-90-089;
DELPHI Collaboration, Z. Phys. **C54** (1992) 55.

- [20] S. Catani, Yu.L. Dokshitzer, M. Olsson, G. Turnock, B.R. Webber, *New Clustering Algorithm for Multijet Cross Sections in e^+e^- Annihilation*, Cavendish-HEP-91/5 published in (but 2 important equations are missing):
S. Catani, Yu.L. Dokshitzer, M. Olsson, G. Turnock, B.R. Webber, Phys. Lett. **B269** (1991) 432.
- [21] S. Catani, private communication.
- [22] OPAL Collaboration, Z. Phys. **C68** (1995) 179.
- [23] ALEPH Collaboration, Phys. Lett. **B384** (1996) 353.
- [24] TASSO Collaboration, Z. Phys. **C47** (1990) 187.
- [25] L. Lönnblad, *ARIADNE 4.4 Program and Manual*, Comp. Phys. Comm. **71** (1992) 15.
- [26] ALEPH Collaboration, Phys. Lett. **B346** (1995) 389.
- [27] JADE Collaboration, Phys. Lett. **B213** (1988) 235.
- [28] S. Bethke, Z. Kunszt, D.E. Soper, W.J. Stirling, Nuclear Physics **B370** (1992) 310.